

1 **Middle Neoproterozoic (Tonian) polar wander of South**  
2 **China: Paleomagnetism and ID-TIMS U-Pb**  
3 **geochronology of the Laoshanya Formation**

4 **Justin Tonti-Filippini<sup>1,2</sup>, Boris Robert<sup>3,4</sup>, Élodie Muller<sup>5,6</sup>, André N. Paul<sup>7</sup>,**  
5 **Fabian Dellefant<sup>1</sup>, Michael Wack<sup>1</sup>, Jun Meng<sup>8</sup>, Xixi Zhao<sup>9</sup>, Urs Schaltegger<sup>7</sup>,**  
6 **and Stuart A. Gilder<sup>1</sup>**

7 <sup>1</sup>Dept. of Earth and Environmental Sciences, Ludwig Maximilians Universität, Munich, Germany

8 <sup>2</sup>Centre for Planetary Habitability, University of Oslo, Oslo, Norway

9 <sup>3</sup>Centre for Earth Evolution and Dynamics, University of Oslo, Oslo, Norway

10 <sup>4</sup>GeoForschungsZentrum Potsdam, Potsdam, Germany

11 <sup>5</sup>Université de Paris, Institut de physique du globe de Paris, CNRS, F-75005 Paris, France

12 <sup>6</sup>IFP Energies Nouvelles, 1-4 Avenue du Bois Préau, 92852 Rueil-Malmaison, France

13 <sup>7</sup>Dept. of Earth Sciences, Université de Genève, Geneva, Switzerland

14 <sup>8</sup>School of Earth Sciences and Resources, China University of Geosciences, Beijing, China

15 <sup>9</sup>IUGS Deep-time Digital Earth program, 88 South Yuhu Road, Kunshan 215300, Jiangsu, China

16 **Key Points:**

- 17 • High-precision ID-TIMS U-Pb dating yields deposition ages of the Laoshanya For-  
18 mation (Yangjiaping, South China) between 809 and 804 Ma.  
19 • Discordant paleomagnetic directions in the red beds are a conflation of three tem-  
20 porally distinct field records residing in hematite.  
21 • Our results do not support rapid true polar wander or abnormal magnetic field  
22 geometry around 805 Ma.

---

Corresponding author: Justin Tonti-Filippini, [justinto@uio.no](mailto:justinto@uio.no)

**Abstract**

Paleomagnetic records of middle Neoproterozoic (820-780 Ma) rocks display high amplitude directional variations that lead to large discrepancies in paleogeographic reconstructions. Hypotheses to explain these data include rapid true polar wander, a geomagnetic field geometry that deviates from a predominantly axial dipole field, a hyper-reversing field (>10 reversals/Ma), and/or undiagnosed remagnetization. To test these hypotheses, we collected 1057 oriented cores over a 85 m stratigraphic succession in the Laoshanya Formation (Yangjiaping, Hunan, China). High precision U-Pb dating of two intercalated tuff layers constrain the age of the sediments between 809 and 804 Ma. Thermal demagnetization isolates three magnetization components residing in hematite which are not time-progressive but conflated throughout the section. All samples possess a north and downward directed component (in geographic coordinates) at temperatures up to 660°C that is ascribed to a Cretaceous overprint. Two components isolated above 660°C reveal distinct directional clusters: one is interpreted as a depositional remanence, while the other appears to be the result of a mid-Paleozoic (460-420 Ma) remagnetization, which is likely widespread throughout South China. The high-temperature directions are subtly dependent on lithology; microscopic and rock magnetic analyses identify multiple generations of hematite that vary in concentration and distinguish the magnetization components. A comparison with other middle Neoproterozoic paleomagnetic studies in the region indicates that the sudden changes in paleomagnetic directions, used elsewhere to support the rapid true polar wander hypothesis (ca. 805 Ma), are better explained by mixtures of primary and remagnetized components, and/or vertical axis rotations.

**Plain Language Summary**

Paleomagnetic directions recorded in 820-780 million year old rocks from South China exhibit large amplitude changes that vary rapidly, which have been interpreted to indicate extraordinarily fast motion of Earth's crust and mantle, up to 90° within a five million year span, with respect to the spin axis of the core. This hypothetical phenomenon, called rapid true polar wander, could be responsible for dramatic global environmental change at that time. To test this theory, we collected over 1000 samples from a well exposed section where the incongruous directions are found. Our measurements suggest that some of the rocks acquired a new magnetic signal during a pervasive remagnetization event in South China around 440 million years ago, long after original deposition of the rocks. New hematite growth has a demagnetization spectrum that partially overlaps or completely obscures the original magnetic signal, which was previously unrecognized. This implies that rapid true polar wander is likely an artefact of magnetic overprinting in ancient rocks from South China. Our results suggest that South China was in a relatively stable position at high latitudes 809-804 million years ago. We find no evidence to support exceptionally fast continental drift or an abnormal geomagnetic field geometry during that time.

**1 Introduction**

Magnetic directions preserved in rocks and sediments can be used to estimate past positions of the geomagnetic pole, known as virtual geomagnetic poles (VGPs). A sequence of rocks spanning several million years in time may record progressive changes in VGP position, which can be used to construct an apparent polar wander path (APWP). APWPs represent the combined effect of tectonic plate motion and the net rotation of the mantle and crust with respect to Earth's rotational pole, called true polar wander (Evans, 2002). A key assumption is that Earth's magnetic pole aligns with the geographic (spin) axis, which is known as the geocentric axial dipole (GAD) hypothesis. If the GAD hypothesis is valid, then APWPs can be used to determine past locations of tectonic plates

72 and reconstruct cycles of continental assembly and breakup; globally correlated APWPs  
73 can be used to estimate rates of true polar wander.

74 A key challenge in paleomagnetism is to build accurate APWPs back into the Pre-  
75 cambrian (Kodama, 2013). Of particular interest is the Neoproterozoic Era, which saw  
76 the end of prolonged geological stasis between 1.8 – 0.8 Ga, a period of relative environ-  
77 mental stability and low tectonic activity referred to as the Boring Billion (N. M. Roberts,  
78 2013), as well as intermittent episodes of Snowball Earth and extreme greenhouse con-  
79 ditions (Hoffman et al., 1998), culminating in the Cambrian explosion and diversifica-  
80 tion of complex life after ca. 542 Ma (Marshall, 2006). An explanation of Earth’s pa-  
81 leogeography and unique climatic behaviour in the Neoproterozoic is crucial for discern-  
82 ing drivers of long-term climate change and biological evolution. Central to this chal-  
83 lenge is unravelling the assembly and breakup of the hypothesized supercontinent of Ro-  
84 dinia between 900 and 750 Ma (Z. X. Li et al., 2008), but Rodinia’s existence and pa-  
85 leogeography are still debated. Torsvik (2003) described Rodinia as ‘a jigsaw puzzle where  
86 we must contend with missing and faulty pieces and have misplaced the picture on the  
87 box’. The South China Block (SCB) constitutes one of the most enigmatic puzzle pieces,  
88 whose Neoproterozoic history has plagued efforts to build a cohesive model of Rodinia  
89 (Evans et al., 2016; Cawood et al., 2020; Jing et al., 2021; Park et al., 2021).

90 Resolving the position and orientation of the SCB in the Neoproterozoic, partic-  
91 ularly around 820 – 800 Ma, is complicated by the apparent occurrence of one or two  
92 rapid true polar wander (TPW) events which may have rotated Earth’s mantle and litho-  
93 sphere 55 – 90° with respect to the spin axis (e.g., Z. X. Li et al., 2004; Niu et al., 2016;  
94 Jing et al., 2020). Large-scale oscillating TPW events (e.g., Fig. 1a), known as inertial  
95 interchange true polar wander (IITPW), have been postulated to resolve discordant pa-  
96 leomagnetic directions from other continents and linked to dramatic global environmen-  
97 tal change observed around the same time (Kirschvink et al., 1997). Sudden directional  
98 changes observed in South China compare well with similar paleomagnetic observations  
99 from Svalbard (Malooof et al., 2006), which have been correlated with the onset of a global  
100 negative carbon isotope anomaly, the Bitter Springs Stage, known as the Bitter Springs  
101 TPW hypothesis (Swanson-Hysell et al., 2012).

102 The debate over South China’s position in Rodinia is linked to the Bitter Springs  
103 TPW hypothesis, as paleomagnetic data from the SCB undergo rapid paleolatitude vari-  
104 ations between 820 and 780 Ma. Various reconstructions of Rodinia place the SCB in  
105 a central, marginal or completely isolated position (Fig. 1b). Classic ‘missing link’ mod-  
106 els place the SCB at a low latitude between Laurentia and Australia (e.g., Z. X. Li et  
107 al., 2008), while other models such as SWEAT (Southwest US – East Antarctica) place  
108 the SCB adjacent to India and/or NW Australia, allowing for a direct fit between Aus-  
109 tralia and Laurentia (Yao et al., 2019). It is also possible that South China was entirely  
110 disconnected from Rodinia and occupied a position near the north pole (e.g., Park et al.,  
111 2021). Increasingly, models appear to challenge a SWEAT configuration in the Neopro-  
112 terozoic, although more and more studies suggest that Australia, India and South China  
113 were geographically close through the late Cryogenian to Ediacaran (S. Zhang et al., 2021,  
114 and references therein).

115 Malooof et al. (2006) and Swanson-Hysell et al. (2012) suggested that testing of the  
116 Bitter Springs TPW hypothesis necessitates robust paleomagnetic and geochronologic  
117 studies of continuous sedimentary sequences from several cratons. If the rapid TPW hy-  
118 pothesis is valid, then all strata that span the Bitter Springs Stage [ca. 810 – 800 Ma  
119 Halverson et al. (2022)], should show similar excursions in their isotopic and paleomag-  
120 netic signals. Resolving these discordant paleomagnetic directions, currently observed  
121 only in Svalbard and South China, calls for integrative studies and is an issue of ‘ma-  
122 jor geodynamic significance’ (Evans et al., 2016). Raub et al. (2015) notes that the TPW  
123 events hypothesized by Malooof et al. (2006) are not directly dated so cannot be precisely  
124 correlated with data from South China. This allows for considerable flexibility in pale-

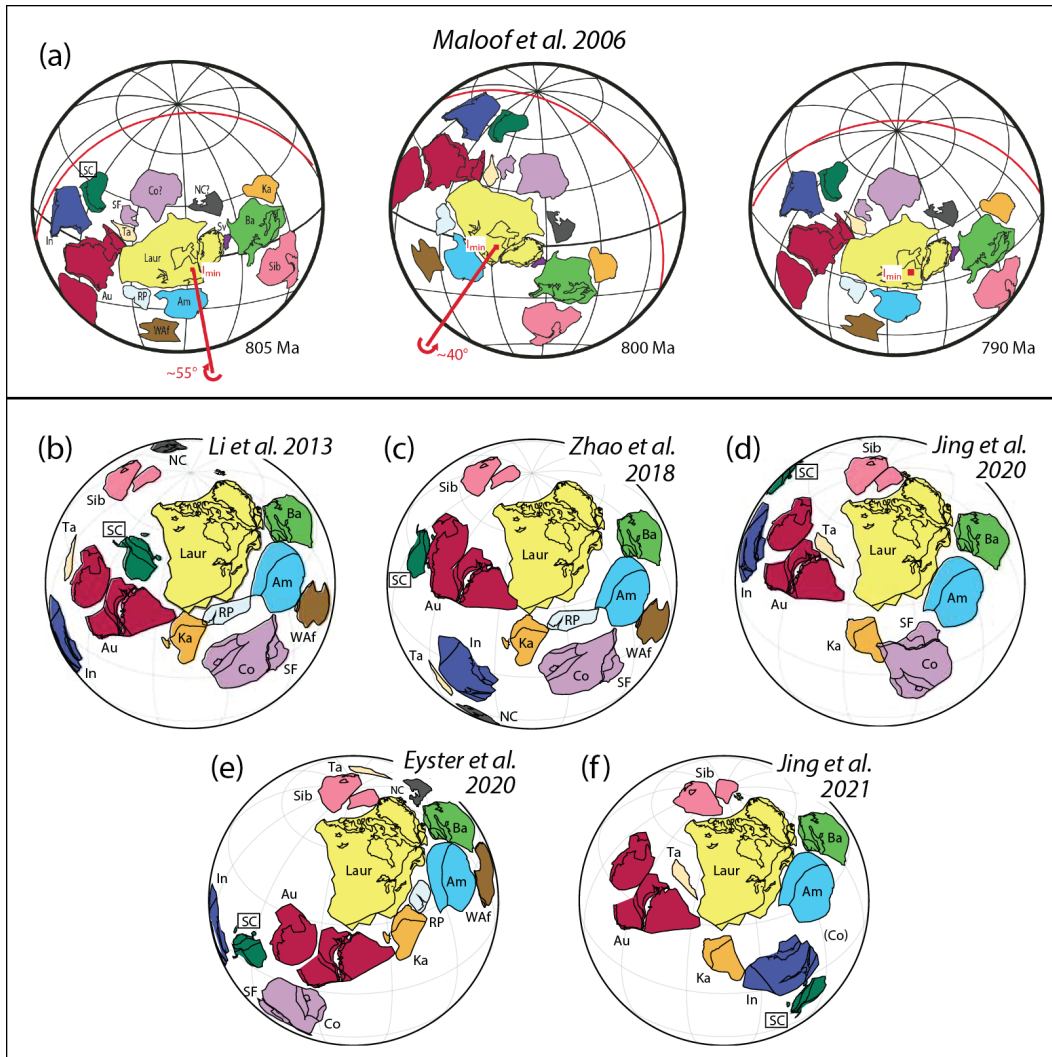


**Figure 1.** (a) Paleogeographic reconstructions of Rodinia during a hypothesized rapid true polar wander (TPW) event between 805 and 790 Ma; the TPW rotation axis ( $I_{min}$ ) is marked in red (after Maloof et al., 2006). (b-f) Proposed reconstructions of Rodinia with Laurentia fixed in present North American coordinates, modified from Evans (2021). South China occupies completely different positions in each reconstruction (see Z. X. Li et al., 2013; Zhao et al., 2018; Jing et al., 2020; Eyster et al., 2020; Jing et al., 2021). Am = Amazonia, Au = Australian cratons including Mawsonland, Ba = Baltica, Co = Congo, In = India, Ka = Kalahari, Laur = Laurentia, NC = North China, RP = Rio Plata, SC = South China, SF = Sao Francisco, Sib = Siberia, Sv = Svalbard, Ta = Tarim, Waf = West Africa.

ogeographic models around 800 Ma, so the TPW hypothesis and the precise configuration of Rodinia ‘must await better constraints’ (Raub et al., 2015).

Other plausible explanations for the discordant paleomagnetic data include rapid tectonic plate motion or non-dipolar to hyper-reversing geomagnetic fields driven by nucleation of Earth’s inner core (e.g., Driscoll, 2016). Peculiar APWPs could also be an artefact of undiagnosed remagnetization. For example, Q. R. Zhang and Piper (1997) warned that South China experienced several episodes of tectonic reworking and suffered extensive sub-tropical weathering, thereby highlighting challenges to paleomagnetism, especially going far back in time. Indeed, numerous studies from South China are based on red sedimentary rocks that have complicated magnetization histories; hence, caution is required when interpreting paleomagnetic signals in red beds.

The Yangjiaping (Hunan Province, China) area has a fairly complete geologic record from the Neoproterozoic through the Paleozoic, including Marinoan tillites and cap carbonates (Macouin et al., 2004). Below the tillites lie the Laoshanya Formation red beds, which were previously dated at Yangjiaping to  $809 \pm 16$  Ma (Yin et al., 2003). There, we collected 1057 paleomagnetic cores in a 85 metre-thick section, freshly exposed along a river, as well as 14 cores in the underlying Lengjiayi Group. We present a paleomagnetic study of those samples, combined with rock magnetic, mineralogical and microscopic analyses, as well as ID-TIMS U-Pb zircon geochronology of intercalated tuffs, in order to shed light on Neoproterozoic geomagnetic field behaviour and the paleogeography of South China around 820 – 800 Ma.

## 2 Geological setting

### 2.1 Nanhua rift basin

The South China Block (SCB) consists of two major tectonic elements, the Yangtze craton to the northwest and the Cathaysia block to the southeast (Fig. 2a), which probably sutured around 1000 – 820 Ma (Cawood et al., 2013), an event referred to as the Jiangnan or Sibao orogeny. There is still controversy over the timing of their amalgamation, but it is generally accepted that the two blocks formed the SCB when they collided along the Jiangshan-Shaoxing suture zone (J. Wang et al., 2015, and references therein). After  $\sim 820$  Ma, during the hypothesized breakup of Rodinia, the Nanhua rift basin developed along the suture zone (S. Zhang et al., 2008), which accumulated sediments through the Neoproterozoic to Early Paleozoic (Charvet, 2013). Several rifting phases likely occurred in the basin as indicated by bimodal magmatism ca. 830 – 820 Ma; the lower sequences are dominated by volcanoclastic sedimentary rocks that are interpreted to be continental rift deposits (J. Wang & Li, 2003).

Rifting terminated in the Nanhua basin in the Late Ordovician to Early Silurian (460 – 400 Ma), perhaps due to inversion of the basin in response to continental convergence (Xu et al., 2016), an enigmatic episode known by several names including the Caledonian (Y. Wang et al., 2007), Wuyi-Yunkai (Z. X. Li et al., 2010) and Kwanghsian (Zheng et al., 2020) orogenic event. We refer to this episode as the Wuyi-Yunkai Orogeny. An explanation for the geodynamic processes that triggered the Wuyi-Yunkai Orogeny is a persistent problem, although an angular unconformity between South China’s pre-Devonian and Devonian strata is widespread (Charvet, 2013). Mid-Paleozoic metamorphic and magmatic rocks, as well as evidence of folding and thrusting, are found throughout the Jiangnan orogen and Cathaysia block, but the tectonic response to the Wuyi-Yunkai Orogeny is not well understood within the Yangtze craton (Zheng et al., 2020).

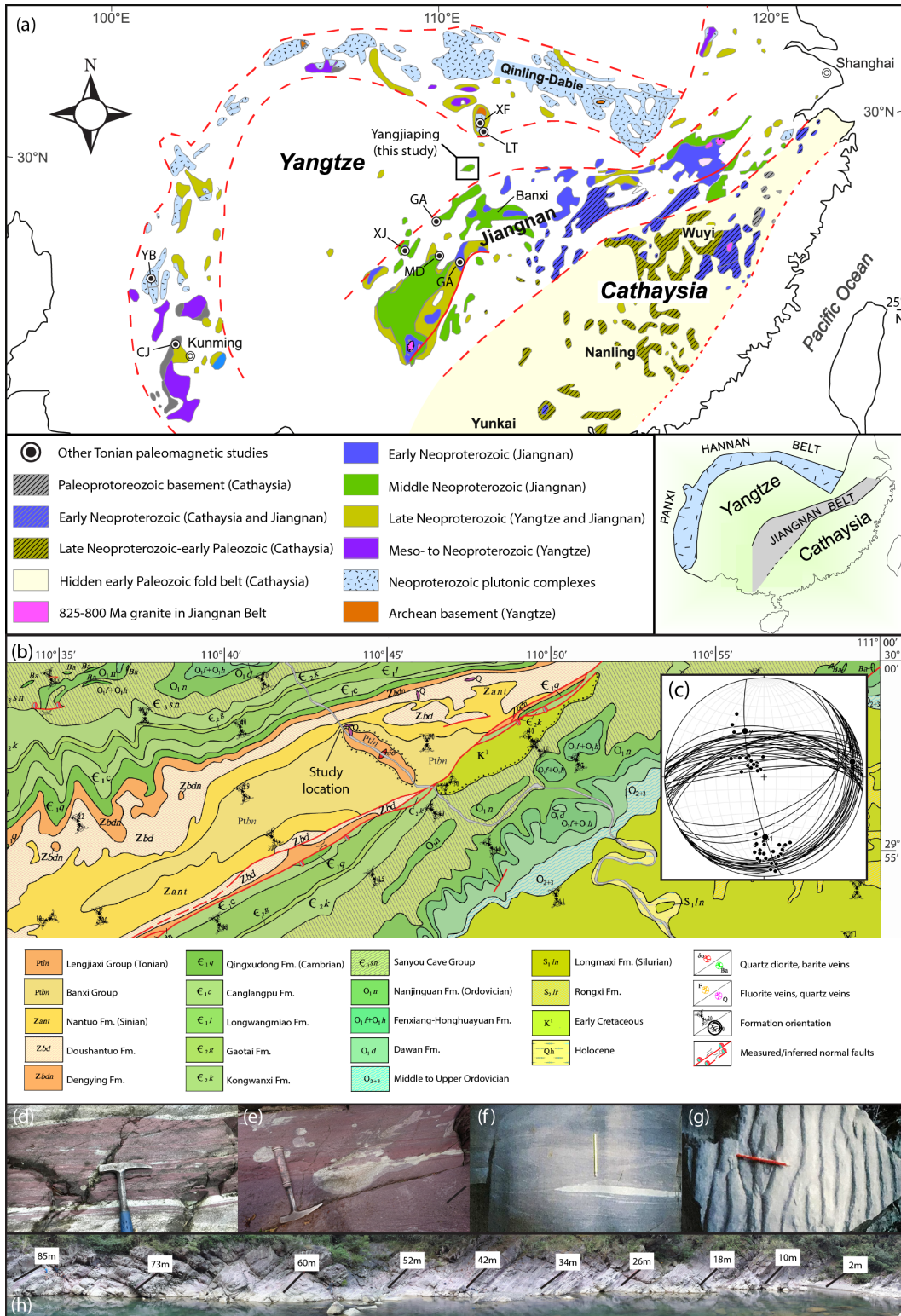


**Figure 2.** (a) Simplified regional map highlighting the Neoproterozoic in South China (after Cawood et al., 2018). Table A1 lists the Tonian studies (black circles with initials). (b) Geological map of the Yangjiaping area, northwest Hunan (after C. Li et al., 2017). (c) Measured bedding strikes and dips in the area indicates near-cylindrical folding, with a slightly plunging ( $11^\circ$ ) axis trending  $80^\circ$ . (d-g) Field photos of the Laoshanya Formation showing (d) alternating green-grey and purple-red sandstones, (e) leaching of the red beds (whitish color) that cuts across bedding, (f) cross-bedding, and (g) ripple marks. (h) Composite photo of sampled section with stratigraphic heights.

171

## 2.2 Banxi group

172

173

174

175

176

177

178

179

180

One of the key rifting successions in the Nanhua basin is the Banxi Group siliclastic sequence (ca. 820 – 730 Ma) that crops out towards the south-eastern edge of the Yangtze craton and is widely exposed in Hunan Province (S. Zhang et al., 2008). The Banxi Group is thought to have formed in an intra-continental rift environment and is characterized by thick sedimentary successions and bi-modal magmatism (Cawood et al., 2018). The Banxi Group in Hunan Province has been considered equivalent to the Danzhou Group in northern Guangxi Province (H. Zhang, 1998) and the Xiajiang Group in eastern Guizhou Province (Lan et al., 2015; Park et al., 2021); however, the age of the base of the Danzhou Group is poorly constrained (Song et al., 2017).

181

182

183

184

185

186

187

188

189

190

Around the study area, the Banxi Group overlies the Lengjiaxi Group with an angular unconformity (the Wuling unconformity), which crops out throughout the orogen and is broadly constrained as 830 – 813 Ma (D. Li et al., 2022). In north-central Hunan, the Cangshuipu Group volcanics were emplaced between the Banxi and Lengjiaxi groups. These volcanics were dated at 824 – 814 Ma (J. Wang et al., 2003; Y. Zhang et al., 2015), which provide an additional constraint on the lower age of the Banxi Group. The Banxi Group consists of the Madiyi Formation in the lower part and the Wuqiangxi in the upper (S. Zhang et al., 2008). The Xihuangshan disconformity (800 – 779 Ma) separates the Madiyi and Wuqiangxi Formations (D. Li et al., 2022), referred to elsewhere as the Zhangjiawan and Xieshuihe Formations, respectively (J. Wang et al., 2003).

191

192

193

194

195

196

197

198

199

200

201

202

203

The Madiyi Formation crops out across Hunan and is thought to have formed in a shallow marine, oxidizing environment. In northwest Hunan, the formation comprises alternating sequences of distinct dark purple-red mudstones and green sandstones (Fig. 2h). A regional study of detrital zircons in the Madiyi Formation yielded age peaks (lower limits) at  $\sim 808$  Ma in the lowermost part, and 803 – 800 Ma in the uppermost part (D. Li et al., 2022). The Madiyi Formation is characterized as relatively  $\text{Fe}_2\text{O}_3$ -rich, with localized pockets of CaO, and may act as a geochemical barrier in the region:  $\sim 80\%$  of the gold deposits in northwest Hunan are hosted in the Madiyi Formation (S. X. Yang & Blum, 1999). The Laoshanya Formation is synonymous with the Madiyi Formation in Yangjiaping (Yin et al., 2003), although recent work suggested the Madiyi Formation may be slightly younger (Y. Zhang et al., 2015; Xian et al., 2020; Park et al., 2021). We use Laoshanya to refer specifically to the outcrop in Yangjiaping, and Madiyi to refer to the wider formation, as our dating shows them to be the same age (Section 4.1).

204

## 2.3 Yangjiaping section

205

206

207

208

209

210

211

212

213

214

215

216

The Yangjiaping section lies in the northwestern Nanhua rift basin (Fig. 2b) (X. Zhang et al., 2000; Song et al., 2017). Yangjiaping is an important landmark for the Precambrian geology of South China and was selected as a ‘candidate stratotype section’ for the Nanhua system (Yin et al., 2003). At Yangjiaping, the Laoshanya Formation is 148 metres thick (Yin et al., 2004) and presents a continuous sequence of alternating purple-red and green-grey sandstones and siltstones (Fig. 2d). For comparison, Madiyi in the southeast part of the basin may be 3500 metres thick (S. Zhang et al., 2008). The Laoshanya Formation is well-preserved and shows evidence of a shallow marine, near-shore or tidal environment, with cross-bedding (Fig. 2f) and ripple marks (Fig. 2g). Some beds contain sub-vertical quartz and calcite veinlets up to several centimetres wide. White to pale green ‘mottling’ is ubiquitous (Fig. 2e), often cross-cutting the purple beds, which may be evidence of localized leaching of iron by secondary fluids (Parry et al., 2004).

217

218

219

220

221

The Laoshanya Formation is conformably overlain by the Xiushuihe (Wuqiangxi) Formation (Fig. 3), dated at  $758 \pm 23$  Ma by the Sensitive High Resolution Ion Microprobe (SHRIMP) method (Yin et al., 2003). Twelve metres below the Xiushuihe/Laoshanya contact lies a tuff whose SHRIMP zircon U-Pb date constrained the upper age of the Laoshanya Formation to  $809 \pm 16$  Ma (Yin et al., 2003). The Laoshanya Formation (strike/dip =

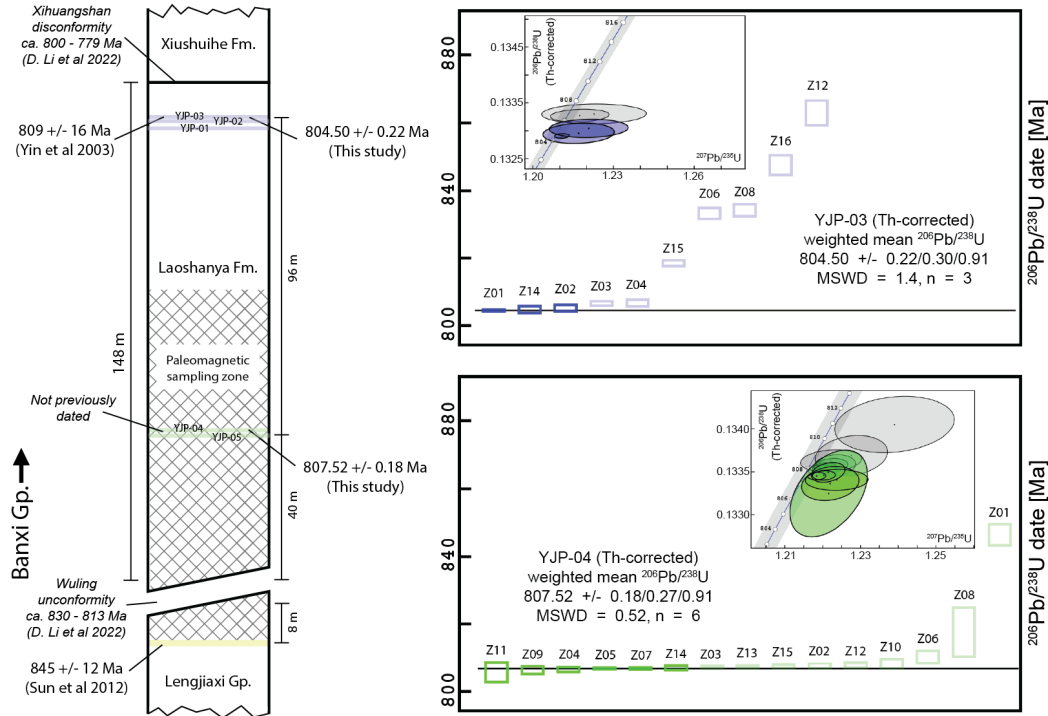


**Figure 3.** Geochronology of the Laoshanya Formation in Yangjiaping with locations of interbedded tuffs (blue, green and yellow stripes). A five metre thick conglomerate marks the base of our section, below which 14 cores were sampled in the Lengjiaxi Group. Previously published dates are shown on the left side of the column; our new dates (YJP-03 and YJP-04) are shown on the right. Coloured rectangles indicate Th-corrected  $^{206}\text{Pb}/^{238}\text{U}$  dates for individual zircons with  $2\sigma$  analytical uncertainty; transparent rectangles indicate results excluded from weighted means. Corresponding  $^{206}\text{Pb}/^{238}\text{U} - ^{207}\text{Pb}/^{235}\text{U}$  concordia diagrams are inset.

222  $255^\circ/58^\circ$ ) unconformably overlies the Lengjiaxi Group ( $258^\circ/87^\circ$ ), dated elsewhere at  
 223 860–835 Ma (Y. Zhang et al., 2015). A five metre thick conglomerate distinguishes the  
 224 unconformity, which demarcates the base of our section. SHRIMP U-Pb dating of lam-  
 225 inated tuff from the underlying Lengjiaxi Group in Yangjiaping yielded  $845 \pm 12$  Ma (Sun  
 226 et al., 2012).

227 The Doushantuo Formation ( $599 \pm 4$  Ma) in Yangjiaping yielded a single-polarity  
 228 magnetization that passed a fold test and was interpreted to be primary, indicating a  
 229 low-latitude position for South China in the Ediacaran (Macouin et al., 2004). However,  
 230 S. Zhang et al. (2015) remarked that the formation does not contain the pattern of re-  
 231 versals common for the Ediacaran elsewhere; the paleopole lies close to other Early Cam-  
 232 brian and Silurian poles for South China; and the positive fold test implies only that the  
 233 magnetization is pre-folding and not necessarily primary. Macouin et al. (2004) recog-  
 234 nized the similarity of their pole to Early Silurian poles, although they considered the  
 235 loop in South China’s APWP between the Early Vendian and Silurian to be a robust  
 236 feature and not an artefact of remagnetization. More detailed rock magnetic data sug-  
 237 gested an episode of magnetite dissolution during early diagenesis (Macouin et al., 2012).  
 238 If the pole of Macouin et al. (2004) represents a Silurian remagnetization, then one could  
 239 expect that other pre-Silurian rocks in Yangjiaping are similarly affected.

240 South China was shaped by large-scale Mesozoic deformation in response to the  
 241 collision of the North and South China blocks that ended by the Late Jurassic (Gilder  
 242 & Courtillot, 1997; Yan et al., 2003). This collision likely produced the folding at Yangji-  
 243 aping seen in Fig. 2(b) (Gilder et al., 1999). J. Yang et al. (2021) identified angular un-  
 244 conformities between Middle Triassic and Jurassic strata, and between Cretaceous and  
 245 pre-Cretaceous strata 20 – 40 km south of Yangjiaping. At Yangjiaping, the Laoshanya  
 246 Formation through the Late Ordovician Wufeng Formation [ $442 \pm 8$  Ma (Xie et al., 2012)]  
 247 have consistent strikes  $250\text{--}280^\circ$  and dips  $55\text{--}70^\circ$ , suggesting a lack of significant de-  
 248 formation until at least the end of the Ordovician. Similarly, no angular unconformity  
 249 exists between the Neoproterozoic Danzhou Group and Ordovician sedimentary rocks  
 250 in northern Guangxi,  $\sim 500$  km to the south (S. Li et al., 2022).

### 251 3 Methods and equipment

#### 252 3.1 Sampling campaigns

253 We collected paleomagnetic samples in September 2019 along a river at Yangjiap-  
 254 ping (Fig. 2b) (Shimen County, Hunan Province) opposite the J01 County Road ( $29.970^\circ\text{E}$ ,  
 255  $110.732^\circ\text{N}$ ). 1057 oriented cores, 2.2 cm in diameter, were drilled over a stratigraphic thick-  
 256 ness of 85 m starting at the base of the Laoshanya Formation (Fig. 3), with a nominal  
 257 spacing of 5-10 cm; occasionally we drilled 4 or 5 cores in the same horizon with each  
 258 sample separated along strike by 10's to 100's of cm. An additional 14 cores were drilled  
 259 over a stratigraphic thickness of 5 m at the top of the underlying Lengjiaxi Group (be-  
 260 low the conglomerate). All cores were oriented with sun (when possible) and magnetic  
 261 compasses. The median magnetic anomaly from the sun compass was  $-3.4 \pm 0.6^\circ$  ( $n =$   
 262  $269$ ), indistinguishable from that expected ( $-3.7^\circ$ ) from the IGRF2020 model (Alken et  
 263 al., 2021) at Yangjiaping; all compass azimuths were corrected accordingly. In August  
 264 2021, five  $\sim 2$  kg samples were collected from suspected volcanic tuff horizons within the  
 265 Yangjiaping section for U-Pb dating (Fig. 3).

#### 266 3.2 U-Pb geochronology

267 High precision U-Pb zircon dating was performed using chemical abrasion - isotope  
 268 dilution - thermal ionization mass spectrometry (CA-ID-TIMS) at the University of Geneva.  
 269 Mineral separation involved crushing and milling bulk samples to  $<300 \mu\text{m}$ , followed by  
 270 concentration on a Wilfley table, Frantz magnetic separator and heavy liquids (methy-  
 271 lene iodide, density 3.32 g/ml). Crack and inclusion-free zircon crystals were hand-picked  
 272 under a binocular microscope, thermally annealed at  $900^\circ\text{C}$  for 48 hours, and then par-  
 273 tially dissolved in concentrated hydrofluoric acid (HF) at  $210^\circ\text{C}$  for 12 hours in a Parr<sup>TM</sup>  
 274 bomb vessel (Widmann et al., 2019). The partially dissolved grains were then extracted  
 275 and washed in 6N HCl in 3 ml Savillex beakers overnight (min. 12 h) at  $80^\circ\text{C}$ . Individ-  
 276 ual zircons were washed 4x with 7N HNO<sub>3</sub> in 3 ml Savillex beakers placed in an ultra-  
 277 sonic bath. Samples were then transferred into 200  $\mu\text{l}$  Savillex microcapsules, mixed with  
 278 1-2 drops of EARTHTIME <sup>202</sup>Pb-<sup>205</sup>Pb-<sup>233</sup>U-<sup>235</sup>U (ET2535) tracer solution (Condon  
 279 et al., 2015; McLean et al., 2015) and dissolved with 2-3 drops of concentrated HF in Parr<sup>TM</sup>  
 280 digestion vessels at  $210^\circ\text{C}$  for 48 hours. After dissolution, samples were dried at  $120^\circ\text{C}$ ,  
 281 re-dissolved in 3N HCl, and then U and Pb were separated using anion exchange column  
 282 chemistry. Chemical preparation was carried out in a class 100 clean-air facility. U and  
 283 Pb were loaded together on outgassed, zone-refined, Re filaments with a silica-gel/phosphoric  
 284 acid emitter solution (Gerstenberger & Haase, 1997), and measured on either a Thermo  
 285 Scientific Triton TIMS or an IsotopX Phoenix TIMS.

286 The measured isotopic ratios were corrected for interferences of <sup>238</sup>U<sup>18</sup>O<sup>16</sup>O on <sup>235</sup>U<sup>16</sup>O<sub>2</sub>  
 287 using a <sup>18</sup>O/<sup>16</sup>O composition of 0.00205 based on repeat measurements of the U500 stan-  
 288 dard. Mass fractionation of U was corrected using a double isotope tracer with a <sup>235</sup>U/<sup>233</sup>U  
 289 of  $0.99506 \pm 0.00005$  ( $1\sigma$ ). The Pb blank isotopic composition is <sup>206</sup>Pb/<sup>204</sup>Pb = 17.84

290  $\pm 0.37$  ( $1\sigma$ ),  $^{207}\text{Pb}/^{204}\text{Pb} = 15.25 \pm 0.33$  ( $1\sigma$ ) and  $^{208}\text{Pb}/^{204}\text{Pb} = 37.05 \pm 0.90$  ( $1\sigma$ ),  
 291 based on total procedural blank measurements. Repeat analyses of the ET100 solution  
 292 ( $^{206}\text{Pb}/^{238}\text{U}$  date:  $100.173 \pm 0.003$  Ma; Schaltegger et al., 2021) yielded a value of  $100.1678$   
 293  $\pm 0.0046$  Ma (MSWD = 3.2,  $n = 32/40$ ). All zircon  $^{206}\text{Pb}/^{238}\text{U}$  dates were corrected  
 294 for  $^{230}\text{Th}$ - $^{238}\text{U}$  disequilibrium using a  $\text{Th}/\text{U}_{\text{magma}}$  of  $3.5 \pm 1.0$ .

295 To determine the U-Pb age of each tuff we take the youngest cluster of  $\geq 3$  anal-  
 296 yses, assuming the zircons crystallised until the time of eruption and all Pb-loss is mit-  
 297 igated by the chemical abrasion procedure, in line with previous U-Pb ID-TIMS stud-  
 298 ies which show that youngest date clusters are generally a reliable measure for eruption  
 299 age (e.g., Schaltegger et al., 2015; Edward et al., 2023). Older dates are assumed to be  
 300 from recycled zircons or associated with inherited cores, wall rock contamination, and/or  
 301 prolonged growth in magma chambers. We report weighted mean U-Pb age uncertain-  
 302 ties at the  $2\sigma$  level in the format  $A \pm X/Y/Z$ , where  $A$  = weighted mean age,  $X$  = an-  
 303 alytical uncertainty,  $Y$  = combined analytical and tracer uncertainty, and  $Z$  = combined  
 304 analytical, tracer and decay constant uncertainty (Schoene et al., 2006).

### 305 3.3 Paleomagnetism

306 Paleomagnetic samples were measured at the Paleomagnetic Laboratory, Ludwig-  
 307 Maximilians-University (LMU-Munich). Cores were cut into 2 cm high cylindrical spec-  
 308 imens using a non-magnetic saw. Specimens were thermally demagnetized in a magnetically-  
 309 shielded, paleomagnetic oven with an accuracy of  $\pm 1^\circ\text{C}$  (Volk, 2016). Remanent mag-  
 310 netizations were measured using a 2G Enterprises superconducting rock magnetometer  
 311 via the automated SushiBar system (Wack & Gilder, 2012). Before treatment and af-  
 312 ter each heating step, bulk susceptibilities were measured at room temperature with a  
 313 Bartington MS2 susceptibility meter. Repeat measurements on a subset of specimens  
 314 were measured with an Agico JR6 spinner magnetometer to check for consistency. 22  
 315 specimens underwent stepwise alternating field (AF) demagnetization up to 90 mT prior  
 316 to thermal demagnetization, which generally removed  $<10\%$  of the natural remanent mag-  
 317 netization (NRM) so was discontinued. All paleomagnetic measurements were made in-  
 318 side a  $90\text{ m}^3$  magnetically shielded room with an average residual field  $<500$  nT.

### 319 3.4 Rock magnetism

320 Based on the paleomagnetic experiments, select samples were subjected to a suite  
 321 of rock magnetic investigations. Some samples were crushed into powder using a porce-  
 322 lain mortar (unsieved). Hysteresis parameters and isothermal remanent magnetization  
 323 (IRM) acquisition curves in applied fields up to 1.8 mT were measured with a Prince-  
 324 ton Measurements Corporation MicroMag 3900 vibrating sample magnetometer (VSM)  
 325 at LMU-Munich. Low temperature experiments were performed on the same instrument  
 326 down to 77 K with a liquid nitrogen cryostat. Thermal susceptibility curves were mea-  
 327 sured up to  $700^\circ\text{C}$  in air using a Agico MFK1-FA Kappabridge with a CS-4 furnace at  
 328 the University of Oslo. Anisotropy of magnetic susceptibility (AMS) measurements on  
 329 99 non-demagnetized specimens were carried out with an Agico MFK1-FA Kappabridge  
 330 at the University of Tübingen, with a peak field intensity of 200 A/m and an operating  
 331 frequency of 976 Hz. Anisotropy of anhysteretic magnetic remanence (AMR) measure-  
 332 ments were made on the same 99 specimens using the SushiBar at LMU-Munich with  
 333 a peak AF field of 90 mT and a DC bias field of 0.1 mT (Wack & Gilder, 2012).

### 334 3.5 Mineralogical and microscopic analyses

335 25 samples were selected for mineralogical analyses. Polished thin sections were first  
 336 observed using transmitted and reflected light microscopy at LMU-Munich. Scanning  
 337 electron microscopy (SEM) analyses were performed with a Hitachi SU5000 Schottky  
 338 Field-Emission Gun (FEG) SEM (LMU-Munich), and on core slices polished to  $0.5\ \mu\text{m}$

339 with a Zeiss Ultra55 FEG SEM at the Institut de Minéralogie, Physique des Matériaux  
 340 et de Cosmochimie (Paris). Backscattered secondary electron (BSE) images were acquired  
 341 using an angle selective backscattered detector with accelerating voltages of 15 - 20 kV,  
 342 and working distances of 7.5 - 10 mm. Elemental compositions were determined by en-  
 343 ergy dispersive X-ray spectrometry using an EDS QUANTAX detector after copper cal-  
 344 ibration. Semi-quantification of the spectra was achieved using the ESPRIT software pack-  
 345 age (Bruker) and the phi-rho-z method.

346 Results from EDXS elemental composition data obtained by SEM were cross-checked  
 347 with XRD measurements to more confidently identify the mineralogy. Four ~10 g core  
 348 samples were finely ground and homogenized in an agate mortar for X-ray diffraction  
 349 (XRD) at the Institut de physique du globe de Paris (IPGP, France). XRD analyses on  
 350 the powders were performed using a Panalytical Xpert Pro transmission diffractometer  
 351 with a copper anode operated at 45 kV and 40 mA and a slit of 0.5° at a 240 mm ra-  
 352 dius. The  $2\theta$  scan was performed in continuous mode from 4° to 90° ( $2\theta$ ) with steps of  
 353 0.0001°. Peak identification was performed using pattern search on the X-ray diffrac-  
 354 tion database of reference spectra Crystallography Open Database ([http://www.crystallography](http://www.crystallography.net)  
 355 [.net](http://www.crystallography.net)).

## 356 4 Results and observations

### 357 4.1 U-Pb geochronology

358 Samples YJP-01, YJP-02 and YJP-03 lie 12 m below the top of the Laoshanya For-  
 359 mation (Fig. 3). Samples YJP-04 and YJP-05 lie 40 m above the base of the formation,  
 360 near the middle of the paleomagnetic sampling zone, 96 m below YJP-01. Song et al.  
 361 (2017) measured a stratigraphic thickness of 184 m for the Laoshanya Formation in Yangji-  
 362 aping (perhaps along the road); our measurements on the riverside outcrop match the  
 363 stratigraphic thickness of 148 m obtained by Yin et al. (2004).

364 Analyses of 44 individual zircons from the upper three samples (YJP-01 to YJP-  
 365 03) yielded dates predominantly between 863 and 804 Ma based on Th-corrected  $^{206}\text{Pb}/^{238}\text{U}$   
 366 ratios, with minor ( $n < 4$ ) clusters at 1.0, 1.7, 2.0 and 2.4 Ga. Sample YJP-03 yielded the  
 367 youngest age plateau at  $804.50 \pm 0.22/0.30/0.91$  Ma (MSWD = 1.4,  $n = 3$ ), which we  
 368 interpret as the depositional age for this part of the section. YJP-01 and YJP-02 con-  
 369 tained many subhedral or rounded zircons that yielded dates between 861 and 807 Ma,  
 370 with no distinct plateau, which we interpret as inherited or recycled.

371 We analyzed 29 zircons from the lower sample group. Sample YJP-04 contained  
 372 hundreds of pristine euhedral zircons and yielded the youngest age plateau at  $807.52 \pm$   
 373  $0.18/0.27/0.91$  Ma (MSWD = 0.52,  $n = 6$ ), which is interpreted as the depositional age.  
 374 YJP-05 contained large subhedral zircons that yielded scattered dates between 1015 and  
 375 818 Ma, with an age plateau at  $818.91 \pm 0.18/0.27/0.92$  Ma (MSWD = 0.45,  $n = 3$ ).  
 376 Given that YJP-05 is situated only 0.6 m below YJP-04, we consider it unlikely that this  
 377 is a true depositional age as it implies a hiatus of 11.4 Myr which is not supported by  
 378 field observations. Th/U<sub>zircon</sub> ratios for YJP-05 are also lower ( $< 0.75$ ) than those of YJP-  
 379 03 and YJP-04 (generally 0.9 to 1.2), suggesting a different provenance or metamorphic  
 380 overgrowth, and increased likelihood of inheritance. Moreover, a depositional age  $> 814$   
 381 Ma would be superpositionally inconsistent with the inferred ages of the underlying Wul-  
 382 ing unconformity and the Cangshuipu volcanics.

383 Assuming no significant depositional hiatuses exist, these results yield an accumu-  
 384 lation rate of approximately 96 m over 3 Myr (32 m/Myr or 3.2 cm/kyr) for the Laoshanya  
 385 Formation. This value compares well with typical sediment accumulation rates of 1-10  
 386 cm/kyr [10-100 m/Myr] for the Neoproterozoic (Sadler, 1981). Our results also agree well  
 387 with the regional compilation of D. Li et al. (2022) who reported age peaks in detrital  
 388 zircons at ~ 808 Ma for lower Madiyi and 803 to 800 Ma for upper Madiyi. Using lin-

**Table 1.** Summary of paleomagnetic results from Yangjiaping (29.970°N, 110.732°E). n = number of specimens. D and I are declination and inclination in (g) geographic (in situ) and (s) stratigraphic (tilt-corrected) coordinates (°).  $\kappa$  and  $\alpha_{95}$  are the precision parameter and 95% confidence ellipse (Fisher, 1953). Pos./neg. rev. test = positive or negative reversal test after McFadden and McElhinny (1990).

Name	n	D <sub>g</sub>	I <sub>g</sub>	D <sub>s</sub>	I <sub>s</sub>	$\kappa$	$\alpha_{95}$	Comments
Lengjiayi Gp.								Strike/dip = 258/87
Lengjiayi A	14	24.6	58.3	7.8	-22.2	269.3	2.4	Neg. fold test
Laoshanya Fm.								Strike/dip = 255/58
Laoshanya A	1002	24.5	55.9	5.9	4.1	29.3	0.8	Neg. fold test
Laoshanya B	100	33.8	-61.9	133.8	-46.9	15.8	3.7	
Laoshanya C	81	149.4	42.5	30.3	73.8	33.6	2.8	Neg. rev. test
Laoshanya C*	44	150.9	43.4	25.4	74.1	48.3	3.1	Pos. 'B' rev. test

\*Filtered for specimens that decay linearly to the origin and have MAD < 10° (Fig. A3).

ear extrapolation (Blaauw & Christeny, 2011), our findings suggest that the Laoshanya Formation was deposited between 808.7 [median, 95% range = 809.6-808.0] and 804.2 [median, 95% range = 804.7-803.5] Ma, assuming a constant accumulation rate (Fig. A4), and can be broadly correlated with the lower Madiyi Formation and upper Xiajiang Group. The age of  $807.52 \pm 0.18/0.27/0.91$  Ma in the middle (40 m height) of the paleomagnetic sampling zone is assigned to the paleopole in the following sections.

## 4.2 Paleomagnetic results

1188 specimens were thermally demagnetized up to 680°C with progressive decreases in temperature steps from 100 to 2°C (Fig. 4). Many specimens demonstrated erratic demagnetization behaviour above 660°C which was accompanied by a large (tenfold) increase in bulk susceptibility, indicating alteration. Three coherent components (A, B and C) were identified using principal component analysis (Kirschvink, 1980), as described below and shown in Fig. 4 with summaries in Fig. 5 and Table 1. Specimens often appeared to contain variable concentrations of all three components, which could be resolved and quantified with vector unmixing analyses (Tonti-Filippini & Gilder, 2023). Some samples also contained a spurious component which demagnetized below 100-200°C and generally aligned with the present day field; this is interpreted to be a viscous remanent magnetization (see Butler, 1992, Chapter 3) and not considered further.

### 4.2.1 Components A, B and C

1016 specimens (86%) contained a coherent north and down (in situ coordinates) directed component that unblocked mostly between 100 and 660°C (Figs. 4a and d). This component is referred to as component A and is ubiquitously present in both the Laoshanya Formation (n = 1002) and the Lengjiayi Group (n = 14). Component A often occurs in combination with a higher temperature component (B or C), although in ca. 6% of the specimens, it is the sole magnetization component. A fold test is negative at 99% confidence limits (McElhinny, 1964), indicating component A was acquired after folding.

181 specimens (15%) displayed coherent demagnetization behaviour from 660 to 680°C that decays to the origin on Zijderveld diagrams (Fig. 4b and c). The high-temperature directions form two clusters on a stereonet (Figs. 5b and c), which are referred to as com-

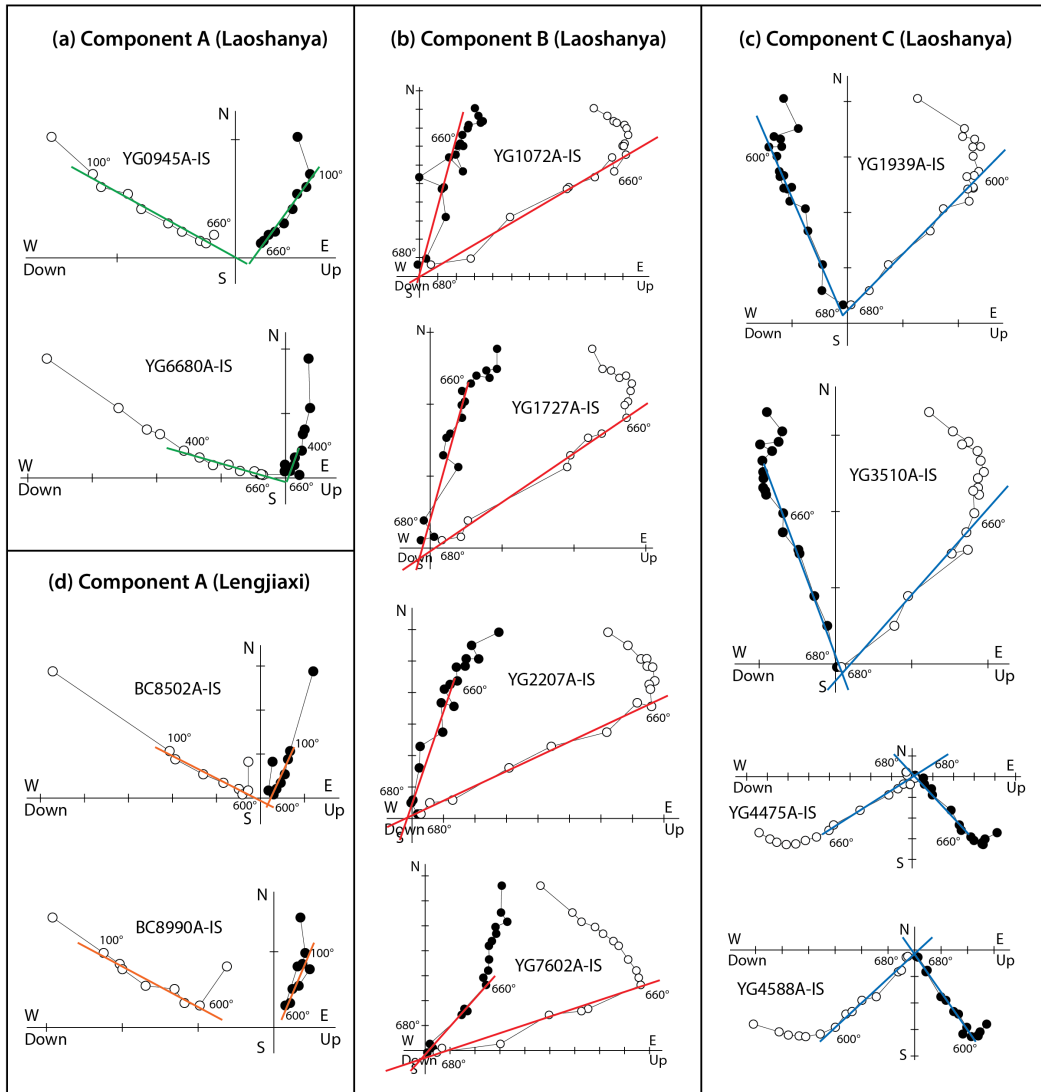


**Figure 4.** Zijdeveld (1967) diagrams of representative samples (in geographic coordinates) from the three component groups (A-C) from the Yangjiaping section displayed with best-fitting ChRM components not forced to the origin. All tick marks are  $10^{-3}$  A/m. In (a), only component A is present, removed below  $660^{\circ}\text{C}$ . Specimens from component B (b) group generally unblock to the origin between  $660$  and  $680^{\circ}\text{C}$  with single-polarity directions, after removal of component A. Component C (c) unblocks to the origin between  $660$  and  $680^{\circ}\text{C}$  and has dual-polarity ChRM directions after removal of component A. (d) Specimens from the Lengjiaxi Group (below the conglomerate) contain component A, but not B or C.

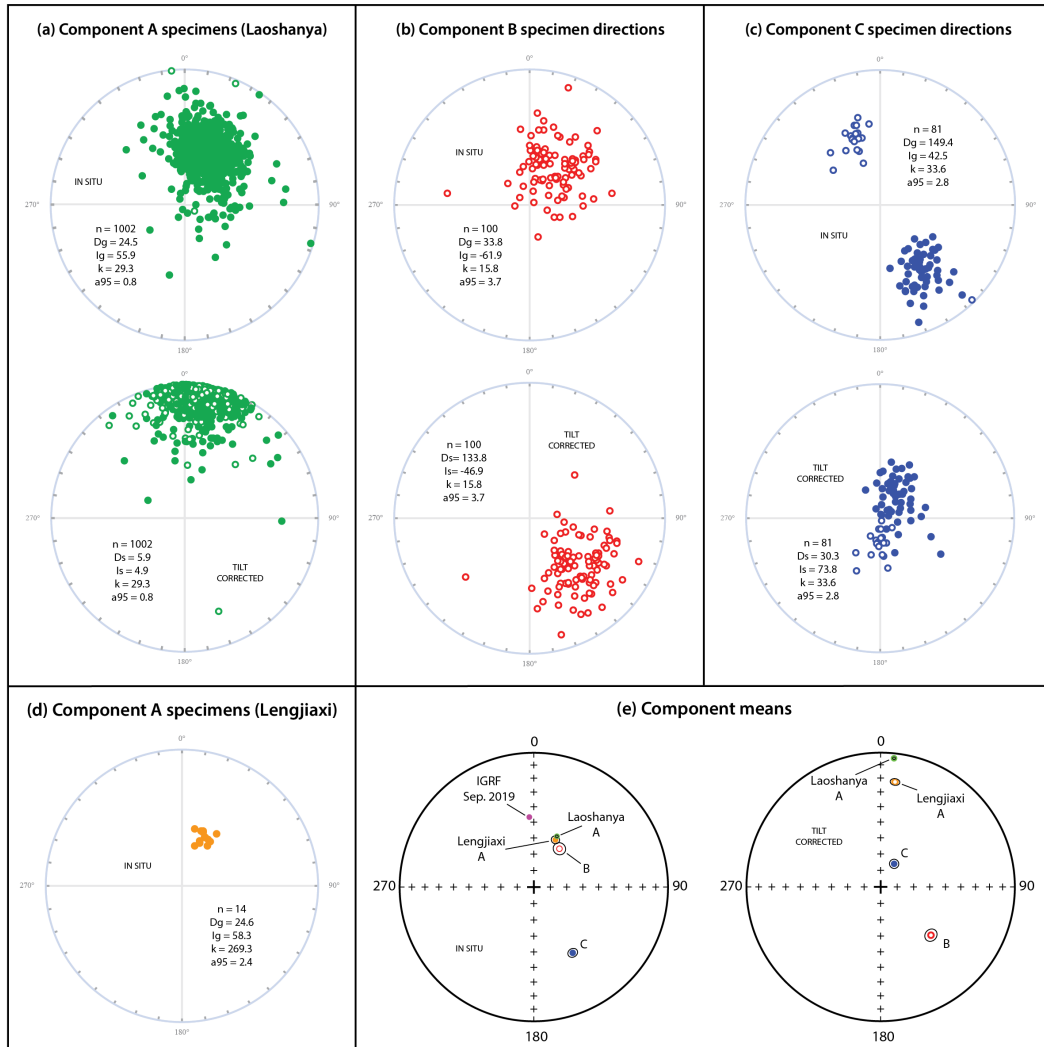


**Figure 5.** Stereonet plots of component A-C paleomagnetic directions in geographic (in situ) and stratigraphic (tilt-corrected) coordinates. Filled circles are lower hemisphere, open circles upper hemisphere. (a-c) Components A and B have a single-polarity while component C has dual-polarities. (d) Specimens from the Lengjiaxi Group only contain component A, indistinguishable to that from the Laoshanya Formation in geographic coordinates. (e) Component mean directions for components A, B and C are distinguishable from the expected IGRF direction (Alken et al., 2021).  $\alpha_{95}$  ellipses are shown in black.

419 ponents B ( $n = 100$ ) and C ( $n = 81$ ). Component B consists of single-polarity, south-  
 420 east and up directions in tilt-corrected (stratigraphic, s) coordinates (Fig. 5b). Despite  
 421 spanning 85 metres of section, component B directions are present only in one polarity.

422 Component C ( $n = 81$ ) comprises dual-polarity directions with steep inclinations  
 423 in tilt corrected coordinates; 62 samples have positive inclinations and 19 negative (Fig.  
 424 5c). A reversal test (McFadden & McElhinny, 1990) is negative at the 95% confidence  
 425 level. However, the reversal test is positive (B classification) if the specimens are filtered  
 426 for the directions that decay linearly to the origin with maximum angular deviations (MAD)  
 427  $\leq 10^\circ$  ( $n = 44$ , Fig. A3). Large MAD values likely arise from unresolved overlapping com-  
 428 ponents (B+C). Components B and C were only found in the Laoshanya Formation so  
 429 no fold test could be performed at the local level. Below, we will perform a regional fold  
 430 test, which is negative for component B and positive for component C.

#### 431 **4.2.2 Sedimentology**

432 Median bed thickness defines three distinct parts (Fig. 6a). In the lowermost 20  
 433 m, median bed thickness ranges from 0.10 to 0.25 m for sandstones and 0.05 to 0.10 m  
 434 for siltstones. This part preserves abundant ripple marks, suggesting a shallow, tidal or  
 435 near-shore environment. Between 20 and 54 m, the median thickness of the sandstone  
 436 beds increases up to 0.35 m. This part contains graded bedding and some cross-bedding,  
 437 indicating more energetic deposition. Median thickness increases towards the top of the  
 438 section (54-85 m) for both siltstones (up to 0.35 m) and sandstones (up to 0.4 m) which  
 439 could indicate a more stable, perhaps deeper, depositional environment; cross-bedding  
 440 and ripple marks are absent. These three parts compare well with stratigraphic units  
 441 1-5 described by Yin et al. (2004).

442 We compared the paleomagnetic results against the stratigraphic log (Fig. 6a) to  
 443 test the correlation between lithology and magnetization components. Specimens con-  
 444 taining component B arise mainly in the siltstone and fine sandstone beds (59%), with  
 445 41% taken from coarse sandstone beds (Figs. 6b and c). 77% of the specimens having  
 446 component C come from coarse sandstones, while 23% come from finer sediments. Com-  
 447 ponent C appears more frequently in the middle part (20-54 m), while component B is  
 448 more abundant in the bottom (0-20 m) and top (54-85 m) parts. The highest density  
 449 of specimens containing component C occurs in the thick sandstone beds between 45 and  
 450 50 m. This is not an artefact of sampling density as the spacing between specimens was  
 451 kept constant at 5-10 cm throughout the section.

#### 452 **4.2.3 Vector unmixing**

453 To quantify component contributions to NRM, we performed vector unmixing anal-  
 454 yses (Tonti-Filippini & Gilder, 2023) on 1152 specimens from the Laoshanya Formation  
 455 (Fig. 7). A goodness of fit (GOF)  $\geq 70\%$  was achieved for 640 specimens using the mean  
 456 component directions from Table 1 and the median demagnetization curves derived by  
 457 Tonti-Filippini and Gilder (2023), i.e., demagnetization data for more than half the spec-  
 458 imens could be accurately modelled by superimposed contributions from components A,  
 459 B and/or C. In the following sections, we grouped the specimens by their dominant com-  
 460 ponent, i.e., the estimated component contribution must be at least  $\sim 40\%$  of the to-  
 461 tal NRM to qualify for that component group. However, 98% of the specimens contain  
 462 some combination of two or three of the components.

### 463 **4.3 Rock magnetic results**

464 Thermal remanence curves for group A samples gradually decay between 100 and  
 465  $660^\circ\text{C}$  (Figs. 4a and d), consistent with fine-grained or pigmentary hematite (Collinson,  
 466 1974). Those in groups B and C show logarithmic decay, unblocking in a narrow range

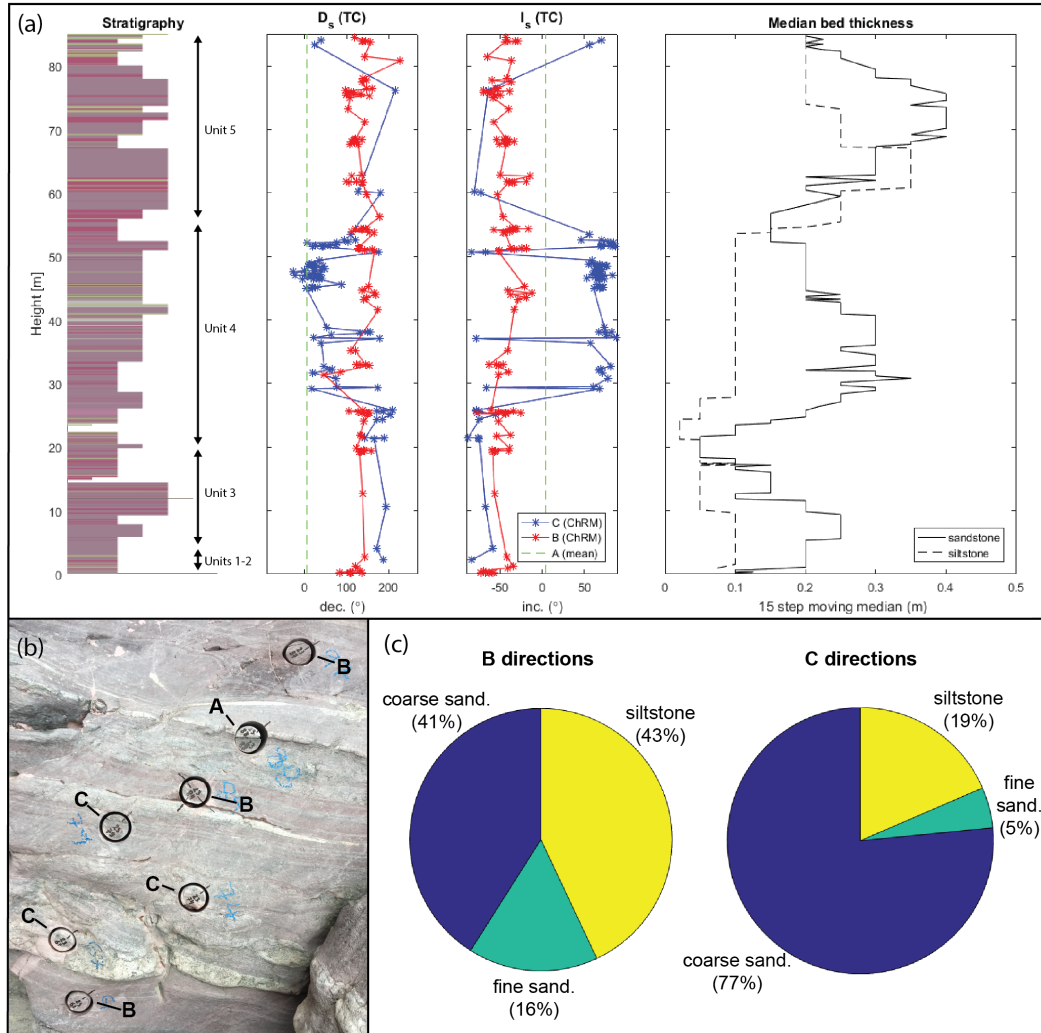


**Figure 6.** Lithological characteristics of paleomagnetic directions. (a) Graphical representation of the paleomagnetic section (Laoshanya Formation, Yangjiaping), with stratigraphic units identified by Yin et al. (2004). The section is shown alongside the paleomagnetic results ( $D_s$  and  $I_s$  = declination/inclination in stratigraphic [tilt corrected] coordinates) and median bed thickness by lithology. (b) Field photo of interbedded siltstone/sandstone that contain the components A-C as indicated. (c) Component C was more frequently identified in the coarse sandstone beds, while component B was found more in siltstones and fine-grained sandstones.

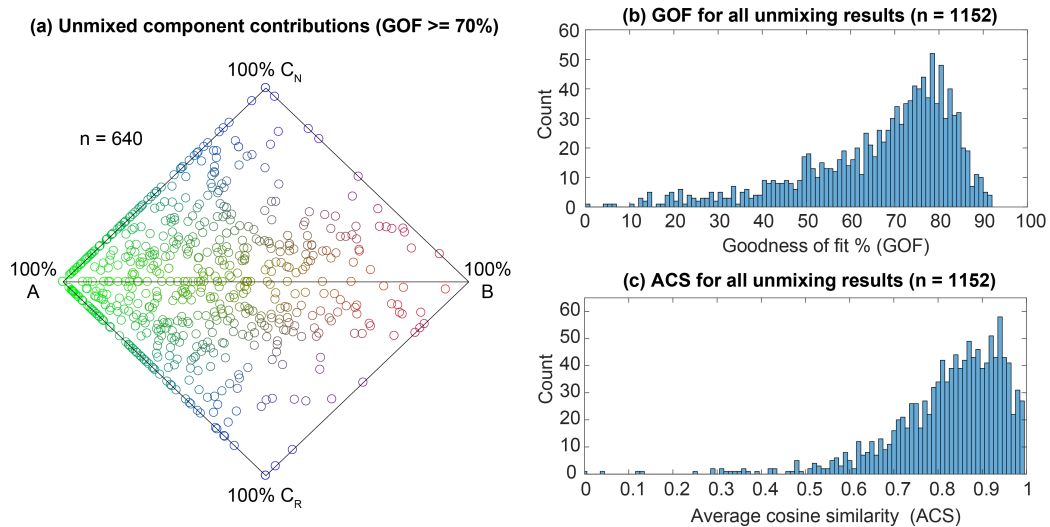


**Figure 7.** Results of vector unmixing analyses. (a) Specimen unmixing results with goodness of fit (GOF)  $\geq 70\%$  ( $n = 640$ ), shaded by component contribution where green = A, red = B and blue = C. Results are shown on a double ternary plot as a proportion of total NRM, unmixed using median component curves derived in Tonti-Filippini and Gilder (2023), representing estimated combinations of components A, B and C<sub>N</sub> (positive inclinations) or C<sub>R</sub> (negative inclinations). Distributions of (b) GOF and (c) average cosine similarity (ACS) for all Laoshanya unmixing results ( $n = 1152$ ).

467 between 660 and 680°C (Figs. 4b and c), consistent with highly crystalline hematite (Özdemir  
 468 & Dunlop, 2002, 2005). To further characterize remanence carriers, we carried out rock  
 469 magnetic experiments on fresh specimens from cores chosen to best represent component  
 470 groups A, B, and C.

#### 471 **4.3.1 High temperature experiments**

472 Fig. 8 shows representative magnetic susceptibility vs. temperature curves (9 out  
 473 of 25 measured). All samples exhibit a rapid decline in susceptibility between 660 and  
 474 700°C, indicative of the Néel temperature in hematite. Another commonality, although  
 475 variable in magnitude, is the existence of a phase with a Curie temperature around 100–  
 476 200°C that is non-reversible upon cooling. This could be indicative of goethite (Till et  
 477 al., 2015) and/or titanium-rich titanohematite (Sprain et al., 2016).

478 The thermal susceptibility curves can be divided into three categories:

- 479 1. Samples in the first category (Figs. 8a-b, d-e and g) have reversible behavior with  
 480 a Hopkinson peak around 660°C, characteristic of single-domain (SD) hematite  
 481 grains (Dunlop, 1974).
- 482 2. Samples in the second category (Figs. 8c and h-i) have irreversible behavior upon  
 483 cooling below 600°C, with a new or enhanced Hopkinson peak around 560°C, near  
 484 the Curie temperature of magnetite. This is indicative of the creation of SD mag-  
 485 netite at high temperatures, which also explains the increase in bulk susceptibil-  
 486 ity above 600°C observed in the thermal demagnetization experiments; the sus-  
 487 ceptibility of magnetite is typically several orders of magnitude higher than hematite  
 488 (O'Reilly, 1984).

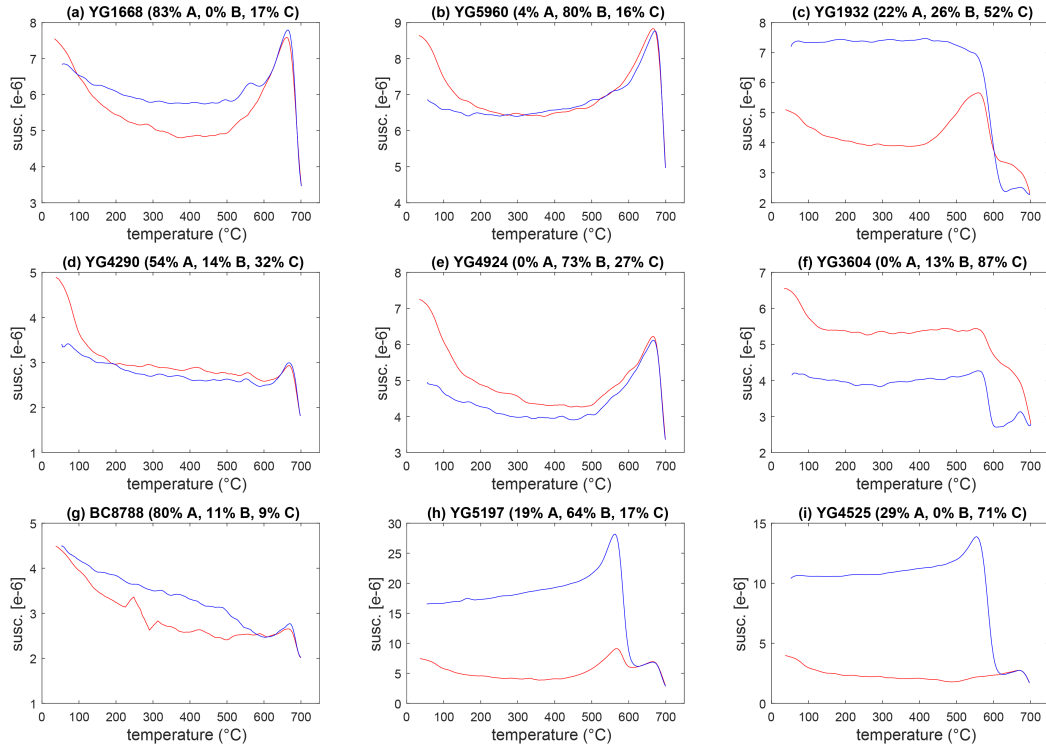


**Figure 8.** Susceptibility (not mass-normalized) vs. temperature curves for each component group between 20 and 700°C (in air) (red lines indicate heating, blue lines cooling). Component contributions estimated by vector unmixing analysis are shown in the subtitles. Most specimens show a Hopkinson peak around 660°C, with rapid decay up to 700°C, consistent with SD hematite. The Hopkinson peaks appear more pronounced in specimens with a dominant (> 50%) component A (a, d, and g) or B (b, e, and h), compared to those with a dominant component C (c, f, and i). Some specimens, e.g., (c), (e) and (i), exhibit a Hopkinson peak upon cooling around 560°C, likely due to the creation of magnetite during heating. All samples have a phase with a Curie temperature below 150°C that is destroyed by heating, which could signal the presence of goethite.

- 489 3. The third category (Fig. 8f) has steep slopes in the cooling curves around 560-  
 490 600°C, indicative of magnetite. However, the susceptibility of the cooling curves  
 491 may be lower than the heating curves, suggesting some pre-existing magnetite was  
 492 oxidized to hematite. At higher temperature, new magnetite was created, some-  
 493 times in lower concentration when the cooling curve is below the heating curve.

#### 494 **4.3.2 Low temperature experiments**

495 Low temperature experiments were performed on the VSM using a liquid nitrogen  
 496 cryostat (Fig. A1). A magnetizing field of 1.8 T was applied at room temperature (293  
 497 K) then switched off. Magnetic remanence was then measured in a null field down to 100  
 498 K and then upon warming to room temperature at a rate of 0.25°/s. Pure hematite typ-  
 499 ically shows a drop in remanence through the Morin transition (Özdemir et al., 2008)  
 500 around ~250 K; however, none of the Yangjiaping samples displayed either a measur-  
 501 able Morin transition or a Verwey transition (characteristic of magnetite), at least un-  
 502 til 100 K (note that temperature stability of the cryostat decreases approaching 100 K).  
 503 Dekkers and Linssen (1989) observed similar low temperature behaviour in natural hematite  
 504 and suggested that impurities (e.g., adsorbed silica) might suppress the Morin transi-  
 505 tion. Small amounts of Ti (e.g., 1 wt.%) can also suppress the Morin transition (Özdemir  
 506 et al., 2008), so the absence of a measurable Morin transition is not uncommon. We found  
 507 no evidence for a Verwey transition in the ca. 100-123 K range indicative of magnetite.

#### 508 **4.3.3 Hysteresis (VSM)**

509 Hysteresis parameters were determined for 28 samples up to 1.5 T (Fig. 9a-c), al-  
 510 though hematite can require >10 T to fully saturate (Rochette et al., 2005). Linear cor-  
 511 rections (75-90% to 1.5 T) were subtracted to account for paramagnetic contributions.  
 512 The corrected hysteresis loops for samples with dominant A or B components (Fig. 9a-  
 513 b) are broad and do not saturate, consistent with single domain (SD) hematite (Özdemir  
 514 & Dunlop, 2014). Samples in group C (Fig. 9c) show narrow wasp-waisted curves, in-  
 515 dicating populations of grains with contrasting coercivity. These wasp-waisted loops are  
 516 similar to multidomain (MD) hematite behaviour observed by Özdemir and Dunlop (2014).  
 517 Compositional variations in titanohematite grains could also explain wasp-waisted hys-  
 518 teresis behaviour (A. P. Roberts et al., 1995), as can mixtures of magnetite and hematite.

519 Samples in group C have bulk coercivities ( $H_c$ ) an order of magnitude lower and  
 520 saturation magnetizations ( $M_s$ ) 2–3 times higher than those in groups A and B (Fig.  
 521 9d). Values of  $H_c$  between 10 and 100 mT in group C imply hematite grain sizes of 10-  
 522 300  $\mu\text{m}$  (Özdemir & Dunlop, 2014), while values between 300 and 600 mT (for groups  
 523 A and B) imply smaller hematite grain sizes, on the order of  $d = 0.1\text{-}3.0 \mu\text{m}$ . Kletetschka  
 524 and Wasilewski (2002) estimated the SD to MD grain size transition at 100  $\mu\text{m}$  for hematite,  
 525 suggesting that the group C hematite is more MD rich than groups A and B. As would  
 526 also be expected for MD hematite, most samples from group C have only minor or non-  
 527 existent Hopkinson peaks (Fig. 8).

#### 528 **4.3.4 Anisotropy (AMS and AMR)**

529 We measured the anisotropy of magnetic susceptibility (AMS) on 99 non-demagnetized  
 530 core specimens (Figs. 10a-e and A2a-c). Anisotropy degrees (P) were <1.1, with max-  
 531 imum axes (K1) trending 235° (on average) in the horizontal plane (tilt-corrected co-  
 532 ordinates). Intermediate (K2) and minimum (K3) axes spread over a NW-SE great cir-  
 533 cle, with some clustering in the vertical and horizontal planes. AMS directions are not  
 534 markedly different among the three groups, although group C has a more pronounced  
 535 tectonic fabric (Fig. 10c). The intermediate tectonic fabrics are typical of sedimentary  
 536 rocks in thrust-and-fold belts (Saint-Bezar et al., 2002). However, the K2-K3 plane im-

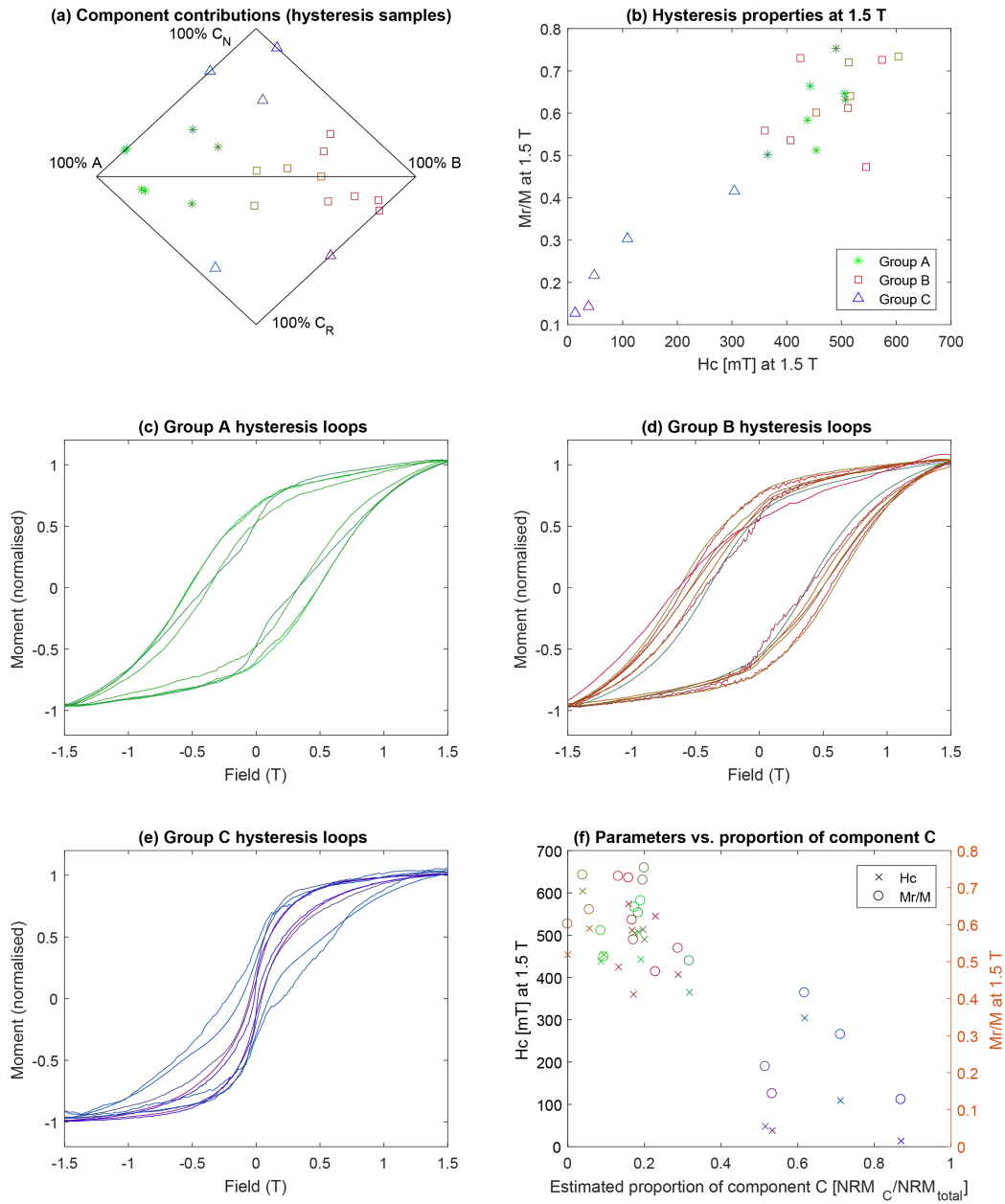


**Figure 9.** High field experiments. (a) Vector unmixing results for samples used in the hysteresis experiments, with dominant components indicated by blue triangles (C), red squares (B) and green stars (A). The same colour shading is preserved in b-f. (b) Samples with higher  $M_r/M_s$  ratios have higher coercive forces ( $H_c$ ). Lower  $H_c$  values can indicate larger hematite grain sizes (Özdemir & Dunlop, 2014), and/or mixtures of magnetite with hematite. (c-e) Room temperature hysteresis curves for specimens from component groups A, B, and C. Groups A and B have wide curves consistent with single domain hematite. Group C has wasp-waisted loops, indicating populations of grains with distinctly different coercivity spectra. (f)  $M_r/M_s$  and  $H_c$  values (at 1.5 T) correlate negatively with the proportion of component C.

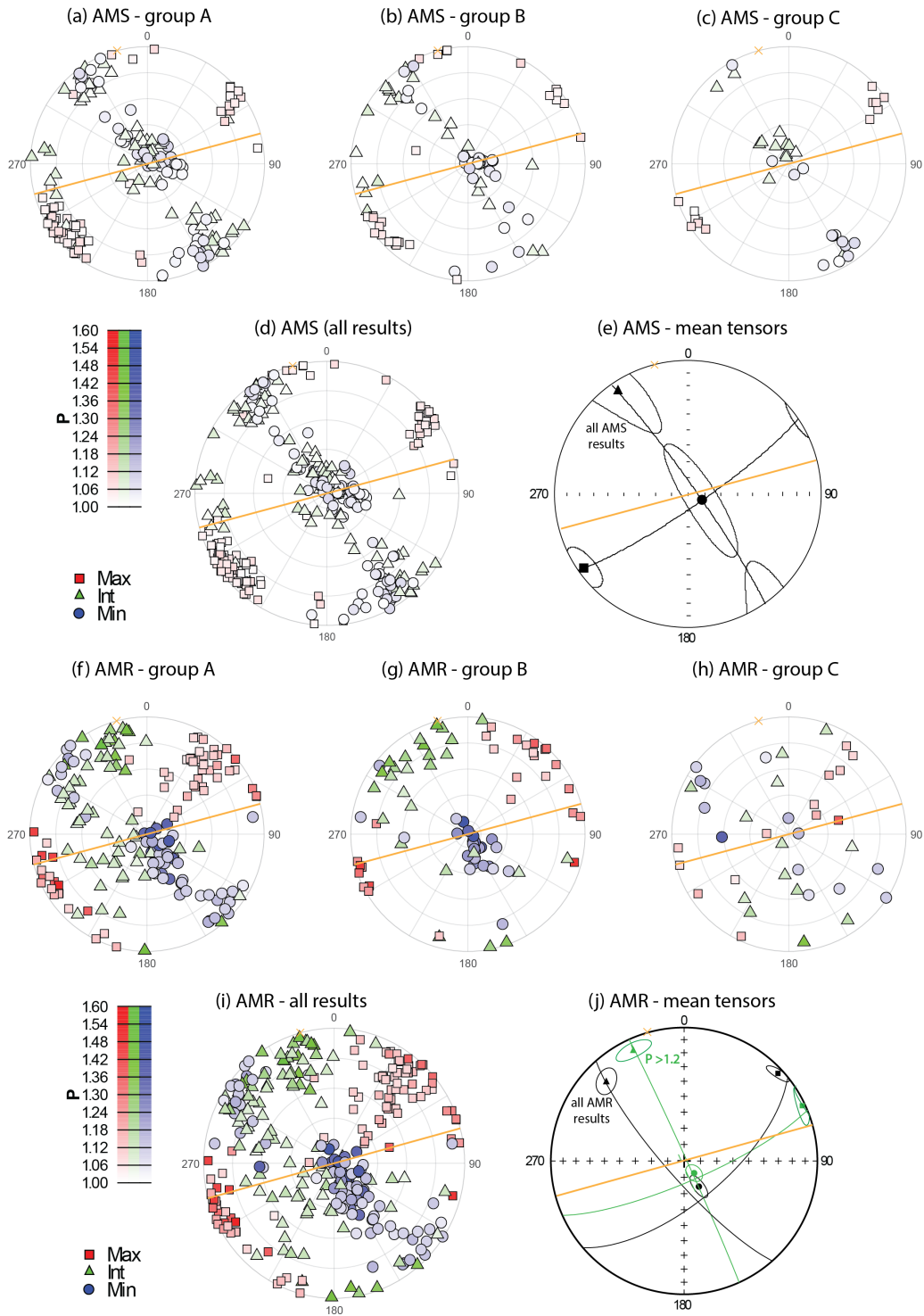


Figure 10. (Caption next page.)

**Figure 10.** (Previous page.) Stereonet plots of principal axis directions for anisotropy of magnetic susceptibility (AMS) and anisotropy of magnetic remanence (AMR) (strike in orange). (a-c) AMS principal axes directions of the three component groups in tilt-corrected coordinates. Groups A and B have sedimentary fabrics (K3, the minor axis, lies perpendicular to the bedding plane) with varying degrees of a tectonic overprint. Maximum anisotropy axes (K1) lie approximately parallel to strike, while some K3 axes are rotated toward the horizontal along a great circle trending perpendicular to strike. Group C records a strong tectonic fabric, with horizontal K3 directions and K2 (intermediate axis) directions perpendicular to bedding. (d) Principal axis directions for all samples, shaded by anisotropy degree (P). (e) The mean K2-K3 plane defines a shortening direction oriented  $325^\circ$ . (f-h) AMR principal axis directions for groups A and B are generally compatible with those from AMS. Group C has mostly incoherent fabrics. (i) Taken together, the most anisotropic samples have AMR K1 directions that parallel more closely to the fold axis direction than AMS (Fig. 2). (j) Mean AMR tensors divided by shape anisotropy. Samples with  $P > 1.2$  are more consistent with the regionally-defined compression axis ( $345^\circ$ ) – all results (black) =  $316^\circ$ , for  $P > 1.2$  (green) =  $335^\circ$ .

537 plies a  $325^\circ$  shortening direction ( $235^\circ$ -trending fold axis), which differs from the mea-  
538 sured strike of our section ( $255^\circ$ ) by  $20^\circ$  (Fig. 10e).

539 Anisotropy of magnetic remanence (AMR) was measured on the same 99 specimens  
540 (Figs. 10f-j and A2d-f) using the refinement method of Wack (2023). Groups A-C have  
541 similar fabrics as AMS, although more scattered (Fig. 10f-h). P values are generally  $< 1.2$   
542 with mean principal axis directions are similar to those for AMS, with maximum axes  
543 (M1) declinations trending  $227^\circ$ , compared to  $235^\circ$  for AMS (K1). Considering all re-  
544 sults together, 29 specimens have  $P > 1.2$  (mean  $P = 1.12$  for  $n = 99$ ). Mean M1 axes  
545 for those ( $P > 1.2$ ) specimens trend  $245^\circ$ ,  $20^\circ$  clockwise relative to the total population  
546 (Fig. 10i and j). The more anisotropic specimens occur in groups A and B, suggesting  
547 they absorbed more of the tectonic stress that produced the deformation in Yangjiap-  
548 ing. This is not surprising since finer-grained sediments (Section 4.2.2) with higher clay  
549 contents typically absorb more tectonic strain (Kodama, 2012).

#### 550 4.4 Mineralogy and microscopy

551 X-ray diffraction peaks are dominated by quartz (25-34 %), albite (12-20 %), mus-  
552 covite (42-54 %) and chlorite (2-5 %) (e.g., Fig. A5). Hematite is the main iron-bearing  
553 mineral whose concentration varies from 2 to 6 wt.%. Chlorites also contain up to 4 %  
554 Fe (EDXS data). SEM observations and EDXS analyses accord well with the XRD data.  
555 SEM images show that fine-grained micas and silicates (chemically consistent with mus-  
556 covite and chlorite) cluster around coarse grains of quartz and alkaline feldspar. Acces-  
557 sory minerals, such as vermicularite, calcite, apatite, zircon, monazite and rutile, were  
558 chemically characterized by EDXS.

559 SEM images (Fig. 11) show abundant hematite in all samples. Fine, needle-like hematite  
560 flakes, generally  $< 1 \mu\text{m}$ , are ubiquitous but more dominant in group A samples (Figs.  
561 11a-f). Samples from groups B and C contain large (30–100  $\mu\text{m}$ ), Ti-rich hematite and  
562 martite (hematite pseudomorphic after magnetite) grains showing trellis textures of ex-  
563 solution typical of Ti-magnetite and/or (hemo-)ilmenites (Figs. 11g-r). Samples from  
564 group B also show abundant 1–2  $\mu\text{m}$  hematite platelets scattered throughout the ma-  
565 trix, or in dense clusters, which presumably replaced and/or oxidized Fe-rich grains (Figs.  
566 11g-k). Larger grains in group B appear to be more leached, with empty Ti-rich (rutile)  
567 lattices left behind, surrounded by hematite platelets (Fig. 11l). Group C samples gen-

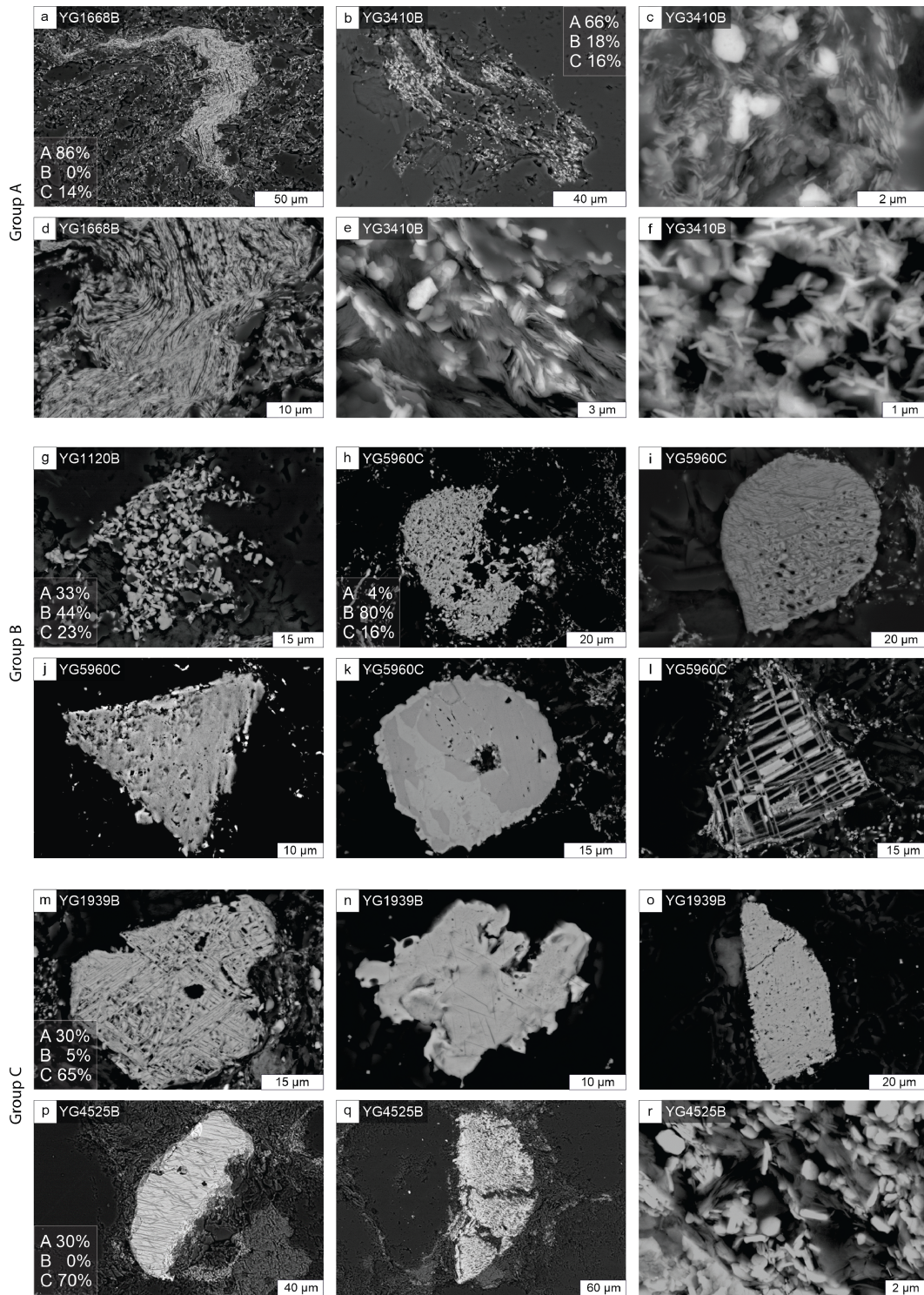


**Figure 11.** SEM images indicating component proportions estimated by vector unmixing analyses. (a-f) Specimens dominated by component A show pervasive Fe remobilization and fine, needle-like hematite flakes, generally  $<1 \mu\text{m}$ . (g-l) Component B-rich specimens contain dense clusters of hematite platelets ca.  $1\text{--}2 \mu\text{m}$  which appear to have formed in situ, perhaps from the leaching of Ti-rich trellis structures. (m-r) Specimens with a high proportion of component C generally have fewer fine-grained hematite flakes and platelets, and are dominated by large ( $30\text{--}100 \mu\text{m}$ ) Ti-rich hematite and martite grains with exsolution features typical of converted Ti-magnetite and/or (hemo-)ilmenite.

568 erally contain fewer hematite flakes in the matrix than the other sample groups (Figs.  
 569 11m-p), consistent with minimal Fe remobilization. Overall, these observations suggest  
 570 there was greater Fe remobilization in groups A and B than in group C.

## 571 **5 Interpretation and discussion**

572 Our experimental results offer several insights into the nature of the remanent mag-  
 573 netizations in the Laoshanya Formation:

- 574 1. SEM analyses show that group C samples contain abundant detrital (ca. 30 – 100  
 575  $\mu\text{m}$ ) Ti-rich hematite grains indicative of MD grain sizes, consistent with an ig-  
 576 neous or metamorphic source (Basu & Molinaroli, 1989), and therefore a primary/detrital  
 577 remanence (DRM). These samples also contained a reduced presence of SD-sized  
 578 ( $< 1\text{-}2 \mu\text{m}$ ) hematite relative to the samples from groups A and B. Hysteresis curves  
 579 for group C samples appear wasp-waisted, indicating distinct magnetic popula-  
 580 tions or dominantly MD grains. Thermal-susceptibility curves for group C also  
 581 showed minor to non-existent Hopkinson peaks, consistent with MD behaviour.
- 582 2. Hysteresis parameters suggest that samples from groups A and B are dominated  
 583 by SD hematite. Thermal-susceptibility curves for groups A and B also show dis-  
 584 tinct Hopkinson peaks. This is supported by SEM observations of abundant sub-  
 585 micron hematite particles in these samples, consistent with Fe remobilization and  
 586 secondary fluid circulation, potentially from the dissolution of Fe-rich minerals (Walker  
 587 et al., 1981). The fact that the SEM images show the SD hematites to be secondary  
 588 products supports a chemical formation, and hence, a CRM.
- 589 3. AMR fabrics indicate group A and B specimens may have absorbed more tectonic  
 590 stress, with higher anisotropy and an inferred strain axis rotated  $20^\circ$  relative to  
 591 the other component groups, consistent with higher clay content/more fine-grained  
 592 material.

### 593 **5.1 Components in the Laoshanya Formation**

594 Of the three magnetization components isolated in this study, component A fails  
 595 the fold test between the Laoshanya and Lengjiaxi formations. The corresponding di-  
 596 rection at 0% unfolding is  $D = 24.5^\circ$ ,  $I = 55.9^\circ$ ,  $a95 = 0.8^\circ$ , composed solely of normal  
 597 polarity, similar to a widespread overprint component found throughout South China,  
 598 originally described by Kent et al. (1987). The corresponding pole at  $\text{lat} = 68.6^\circ\text{N}$ ,  $\text{lon}$   
 599  $= 176.7^\circ\text{E}$ ,  $dp/dm = 0.8^\circ/1.1^\circ$  is near-sided with respect to Cretaceous reference poles  
 600 for South China. The unfolding path of component A intersects the Cretaceous poles  
 601 of B. Huang et al. (2018) at 10-20% unfolding, however, the near-sidedness could also  
 602 be explained by inclination shallowing. Given that the overprint is a CRM and the ref-  
 603 erence poles are based mostly on continental sediments with DRM, one would expect a  
 604 CRM to be immune from inclination shallowing, as found by Meng et al. (2022). Hence,  
 605 we interpret component A to be a Cretaceous overprint acquired during the normal su-  
 606 perchρον [120-83 Ma (Ogg, 2012)].

607 The interpretation of components B and C is more complicated. Taken at face value,  
 608 both components could be primary, as they display near-identical thermal remanence  
 609 behaviour. Fig. 12 plots the corresponding poles in both geographic and stratigraphic  
 610 coordinates, together with a 510 to 120 Ma APWP for South China (B. Huang et al.,  
 611 2018). The component B pole in tilt-corrected (TC) coordinates [LS-B (TC)] lies in prox-  
 612 imity to the 450 Ma segment of the reference APWP. Component B in geographic/in situ  
 613 (IS) coordinates [LS-B (IS)] and the TC and IS poles for component C lie far from the  
 614 reference curve.

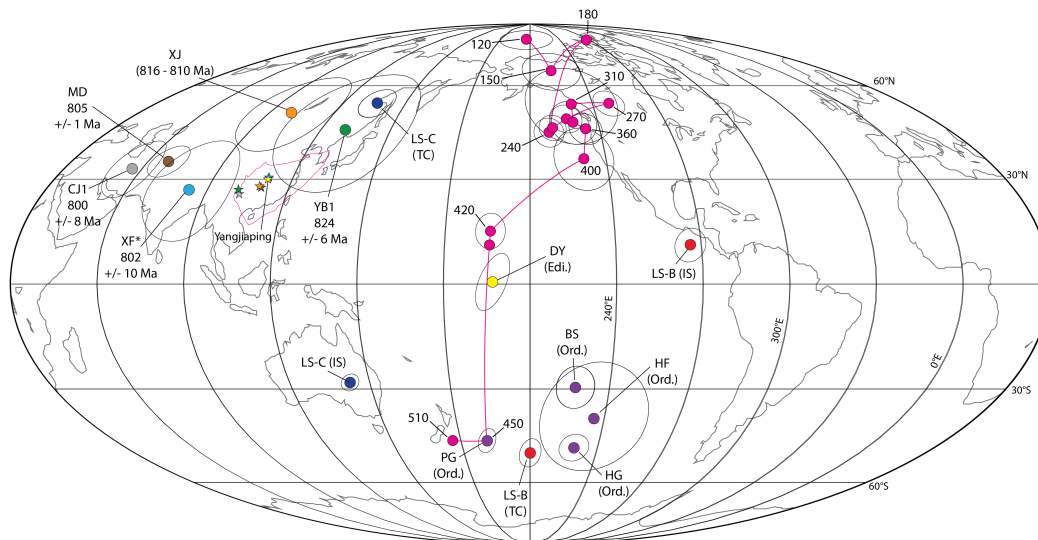


**Figure 12.** Laoshanya (LS) Formation poles from components B and C in in situ (IS) and tilt-corrected (TC) coordinates plotted with the APWP for South China from B. Huang et al. (2018) shown in pink. The LS-B (TC) pole lies close to the 450 Ma segment of the APWP. LS-B (IS) and LS-C (IS and TC) lie far from the reference path. Table A1 provides details of relevant Tonian poles (820-800 Ma). Ordovician (Ord.) poles are shown in purple (Table A2). The Ediacaran (Edi.) pole from the Doushantuo Formation in Yangjiaping (DY) is shown in yellow. Stars indicate site locations.

615 Fig. 12 also plots our data alongside Tonian to pre-Devonian poles from the SCB  
 616 (Tables A1 and A2, assessed in Appendix B). LS-B (TC) lies among several Ordovician  
 617 poles for the SCB. Together with the rock magnetic and microscopic observations (Sec-  
 618 tion 4), we interpret component B to be an Ordovician-aged chemical remagnetization.  
 619 This coincides with a mineralogical study in Yangjiaping that indicates the Banxi Group  
 620 was heated to 260°C in the mid-Paleozoic (H. Wang et al., 2014). Estimated temper-  
 621 atures increase to 360°C towards eastern Hunan and the Jiangnan belt, whose heat source  
 622 was linked to the Wuyi-Yunkai (Caledonian) Orogeny (H. Wang et al., 2016). Moreover,  
 623 Cawood et al. (2018) suggested that the Banxi Group and its equivalents in the Jiang-  
 624 nan Belt were reworked between 460 – 420 Ma, based on metamorphic and petrogenetic  
 625 analyses together with  $^{40}\text{Ar}/^{39}\text{Ar}$  and U-Pb dating across the Wuyi-Yunkai orogen (Z. X. Li  
 626 et al., 2010).

627 The component C pole, LS-C (TC), lies close to Tonian poles from the 824 ± 6 Ma  
 628 Yanbian Dykes (Niu et al., 2016) and 816 – 810 Ma Xiajiang Group (Park et al., 2021).  
 629 The similarity with other Tonian-aged poles, as well as its dual-polarity, lead us to in-  
 630 terpret component C as primary. Reversal frequency in the Tonian (ca. 807.5 Ma) based  
 631 on seven polarity intervals between 20 – 54 m (34 m), where the highest density of com-  
 632 ponent C directions are found (Fig. 6a), yields 0.21 reversals per metre or 6.7 reversals/Myr  
 633 given an accumulation rate of 32 m/Myr. This is a minimum value, as the true number  
 634 could be higher if the signal was obscured by component A or B overprints. Our esti-  
 635 mate for the Tonian is higher than the present rate of 4-5/Myr for the past 5 – 10 Myr  
 636 (Ogg, 2012), but compares well with estimates from the Ediacaran at 6-24/Myr (Meert  
 637 et al., 2016; Hounslow et al., 2018).

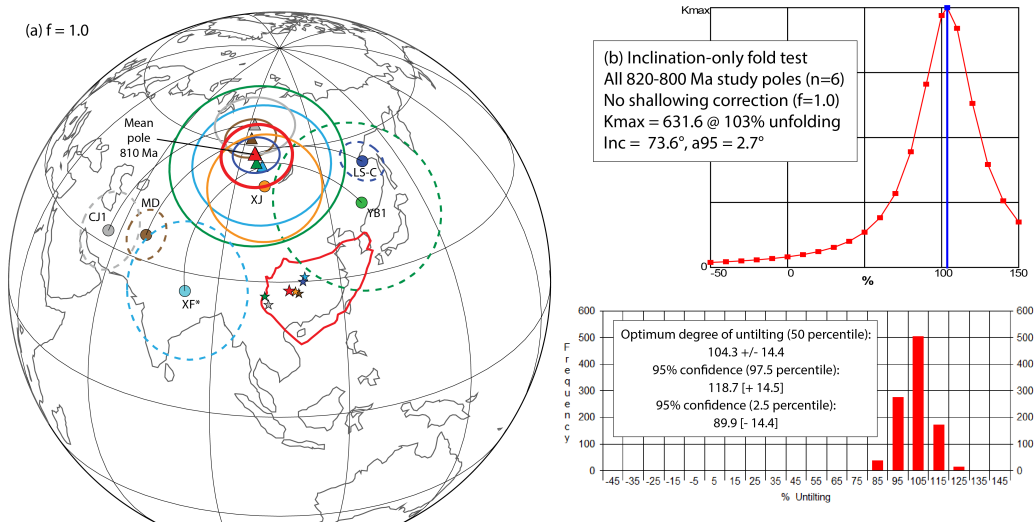


**Figure 13.** Scenario 1: Can vertical axis rotations explain discordant paleomagnetic data in the Tonian? (a) If allowed to rotate, all Tonian poles (820-800 Ma) collapse to define a group pole ca. 810 Ma. XJ was held fixed as its site location (and pole) lies between all the other sites (and poles). The outline of the SCB and the group mean pole are in red. Dashed circles indicate pole locations before vertical axis rotations. Poles are summarized in Table A1 and Appendix B. (b) An inclination-only fold test with parametric sampling (Watson & Enkin, 1993; Enkin & Watson, 1996);  $k$  maximizes at  $104 \pm 14\%$  unfolding.

638

## 5.2 Paleomagnetic poles from South China

639

640

641

642

643

644

645

646

647

648

649

650

651

652

653

654

655

Relevant Tonian (820-720 Ma) poles are assessed in Appendix B. We omitted pole GA of Chang et al. (2022) due to its ambiguous age. We retained the Liantuo (LT1) pole, and assigned it a ca. 780 Ma age following Park et al. (2021), but note that their geochronology yielded several concordant dates significantly younger than 780 Ma including one, at  $748.4 \pm 0.56$  Ma, similar to that used by Evans et al. (2000). We excluded poles CJ3 (Jing et al., 2020) and YB2 (Niu et al., 2016) because they lack reversals and fail the statistical requirements of Meert et al. (2020). Poles XJ, CJ1 and MD were derived from sedimentary rocks; the original studies used a blanket inclination shallowing correction with a flattening factor ( $f$ ) of 0.6 to compute the average pole. Applying the E/I correction method (Tauxe & Kent, 2004) to Laoshanya component C directions ( $n = 81$ ) identifies insignificant inclination shallowing ( $f = 1.0$ ). Our E/I assessment of all 169 specimen data from Park et al. (2021) corrected the mean inclination from  $-72.5^\circ$  to  $-75.7^\circ$ , equivalent to  $f = 0.81$ . Therefore, we see no justification to use  $f = 0.6$  for XJ, CJ1, and MD, and hence, we recomputed the poles without a shallowing correction. Fig. 12 shows that the Tonian poles undergo high amplitude and rapid motion between 820 and 800 Ma. Although some workers have interpreted such variability as reflective of rapid TPW (Park et al., 2021), we consider alternative hypotheses to explain the data.

656

### 5.2.1 Scenario 1: Vertical axis rotations dispel TPW

657

658

659

660

661

Upon first glance, Tonian-aged poles appear widely scattered, potentially consistent with rapid TPW (Fig. 13a). However, the poles appear to be distributed along a small circle centered on the sampling sites. IITPW, as described by Kirschvink et al. (1997), should produce large changes in paleolatitude (i.e., observed inclinations), unless the sampling sites were located close to the axis of the rotation and the minimum moment of

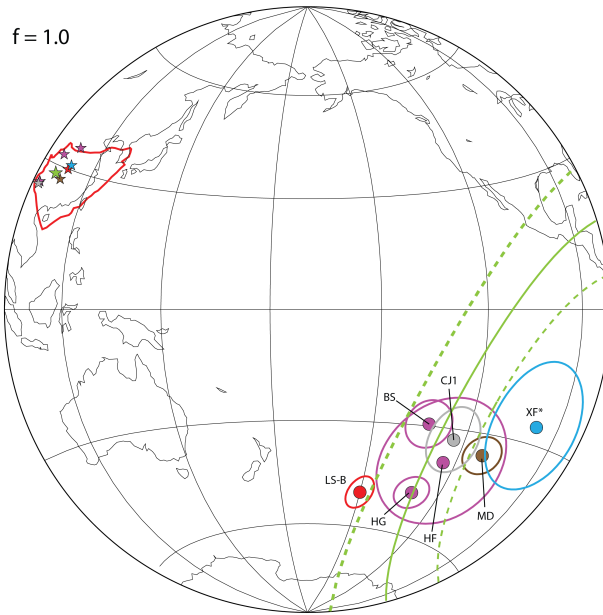


**Figure 14.** Scenario 2: Can an Ordovician remagnetization account for the discordant directions in South China? When plotted in the southern hemisphere, the CJ1, MD and XF\* poles (Table A1) overlap with several Ordovician poles (purple, see Table A2), suggesting they may be affected by remagnetization. No corrections for inclination shallowing were applied. A small circle (green) is plotted through HF, HG and BS poles, centered on the mean site location (PG was excluded from the small circle calculation as it has a significantly different inclination). Dashed lines show 95% confidence limits.

662 inertia (i.e., in an equatorial position at the centre of the supercontinent). The poles for  
 663 South China between 820-800 Ma indicate a high-latitude position but do not show sig-  
 664 nificant changes in inclination, inconsistent with rapid TPW. Although the interior of  
 665 South China experienced only minor rotations ( $<20^\circ$ ) since the Cretaceous (Meng et al.,  
 666 2022), Permo-Triassic rocks exhibit a large variability in declination that matches the  
 667 rotational amplitude of the Tonian data (Tan et al., 2007; Gilder et al., 2008). We there-  
 668 fore entertain the possibility in Scenario 1 that the SCB experienced internal vertical axis  
 669 block rotations that streaked the Tonian poles out about a small circle centered on the  
 670 sampling sites.

671 Under this scenario, all poles are considered to be based on primary, approximately  
 672 coeval magnetizations, obtained at similar paleolatitudes. We arbitrarily kept XJ fixed  
 673 as it passed a regional fold test and its site and pole lie in the middle of the other sites  
 674 and poles. After allowing the other 820-800 Ma poles to freely rotate about their respec-  
 675 tive sampling sites, the poles come into close coincidence (Fig. 13a). If the data were pri-  
 676 mary, a regional fold test on the directions would be meaningless given the dispersion  
 677 in declination, yet an inclination-only fold test would be independent of the differential  
 678 rotations. An inclination-only fold test (Enkin & Watson, 1996) yielded a maximum pre-  
 679 cision parameter  $\kappa_{max}$  at  $104 \pm 14\%$  unfolding with an inclination of  $73.6^\circ$  (Fig. 13b).  
 680 Therefore, by accounting for post-Permian vertical axis rotations, the 820-800 Ma South  
 681 China poles can be explained without the need to invoke rapid TPW, extreme plate mo-  
 682 tion or anomalous field behaviour. We thus calculated a mean pole of  $P_{lat} = 57.8^\circ$ ,  $P_{lon}$   
 683  $= 95.9^\circ$  ( $A_{95} = 7.6^\circ$ ,  $N = 6$  studies) which we consider representative of the Tonian for  
 684 the SCB at ca. 810 Ma.

685

### 5.2.2 Scenario 2: Pervasive Ordovician remagnetization

686

687

688

689

690

691

692

693

694

695

696

697

698

699

700

Scenario 1 provides a convenient explanation for the dispersion of poles between 820-800 Ma, but perhaps misses a potentially important subtlety. In Scenario 2, we consider the possibility that remagnetization is pervasive in the SCB and contributes to the scatter of Tonian poles. We fit a small circle running through three, presumably primary Ordovician poles (HF, HG and BS), centered on their mean site location (Fig. 14a). When plotted in the southern hemisphere, the “Tonian” CJ1, MD and XF\* poles lie near the small circle swath, suggesting that an Ordovician remagnetization may be a common feature that better explains the origin of their remanences. Indeed, the Madiyi (MD) pole was derived from silty mudstones, like component B in the Laoshanya Formation. The Chengjiang (CJ1) study also reports a mid-inclination secondary component (CJ3) which is offset from the primary component (à la Laoshanya components B and C). Therefore, an Ordovician remagnetization advocated in Scenario 2 provides an alternative explanation for the rapid pole variations ca. 805 Ma, whereby some of the magnetization components are wholly or partially overprinted. Large amplitude and rapid TPW would therefore be explained as a mixing of components acquired at distinctly different times.

701

702

703

704

705

706

707

708

709

710

711

712

713

714

Remagnetization could have occurred during a mid-Paleozoic deformation event (i.e. the Wuyi-Yunkai Orogeny). Consistent with this idea, Chang et al. (2022) mapped the Banxi Group as unconformably overlain by Devonian strata, thereby supporting a Ordovician-Silurian deformation event. 90 km to the south-east of Yangjiaping, an angular unconformity occurs at the top of the Middle Ordovician Guniutan Formation (Schmitz et al., 2010), however, near Yangjiaping, the formations above and below the Guniutan Formation have similar bedding orientations. Chen et al. (2014) described a significant hiatus between the Ordovician Wufeng and Silurian Longmaxi (Lungmachi) formations in Zhangjiajie, 100 km south of Yangjiaping. Zheng et al. (2020) dated the onset of this hiatus to  $447 \pm 1.4$  Ma using rhyolitic tuffs in the top of the Wufeng Formation, 30 km to the north of Yangjiaping, and linked the hiatus to deformation/uplift caused by the Wuyi-Yunkai Orogeny. An Ordovician age for the deformation (and remagnetization) is consistent with the apparent age of component B in the Laoshanya Formation (as its pole overlaps several Ordovician poles).

715

716

717

718

719

720

After excluding poles suspected of mid-Paleozoic remagnetisation, an inclination-only fold test for three remaining Tonian poles (XJ, YB1 and LS-C) yields  $\kappa_{max}$  at 102 % unfolding (Fig. 15b). If the remaining poles are allowed to rotate, again with XJ fixed, the resultant mean pole of  $P_{lat} = 55.1^\circ$ ,  $P_{lon} = 98.5^\circ$  ( $A_{95} = 14.8^\circ$ ,  $N = 3$  studies) has a larger (2x) uncertainty and slightly ( $\sim 2^\circ$ ) steeper inclination than the pole derived in Scenario 1 (Fig. 15a).

721

### 5.2.3 Scenario 3: No rapid TPW between 810 and 780 Ma

722

723

724

725

726

727

728

729

730

731

732

733

734

In Scenario 3, we build on the assumption that South China has experienced Phanerozoic deformation leading to vertical axis rotations (Scenario 1), or widespread Ordovician remagnetization (Scenario 2), and explore the implications. The mean 810 Ma poles derived in both scenarios suggests that South China was in a stable, high-latitude position. The next (younger) pole is LT1 dated at 780 Ma which, if primary, lies  $\sim 53^\circ$  away from the 810 Ma poles, implying an approximate APW rate of  $\sim 1.8^\circ/\text{Myr}$  between 810 and 780 Ma. This rate is within estimated rates of conventional TPW ( $< 2.0^\circ/\text{Myr}$ ) since 540 Ma (Torsvik et al., 2012). However, the separation between the poles is mostly in the declination (rotational) component as seen when drawing a small circle centered on the mean sampling site and the 810 Ma pole from Scenario 1. LT1 could also have experienced vertical axis rotations, as the pole lies within 95% confidence limits of the uncertainty of the 810 Ma poles, so the APW could be some combination of conventional TPW, rotation and/or plate motion. In sum, the evidence for rapid TPW between 810

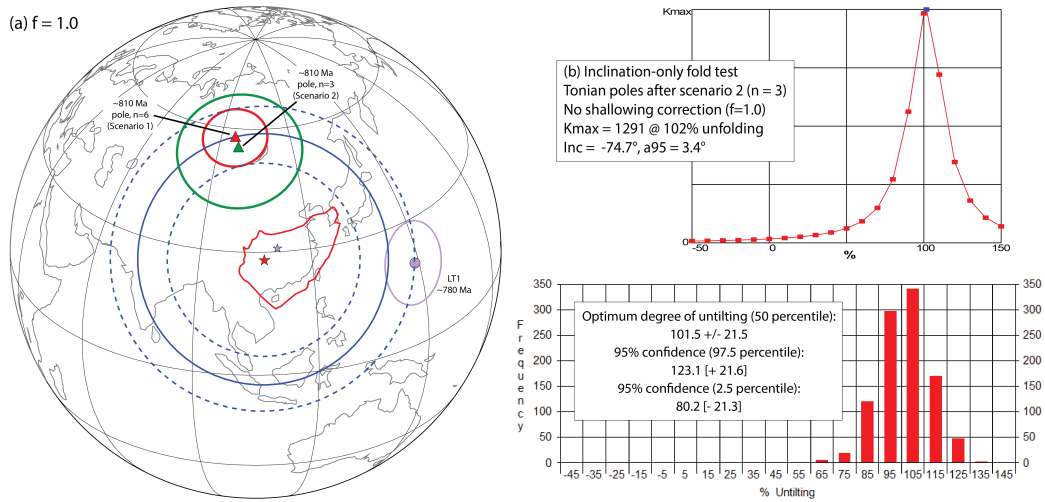


**Figure 15.** Scenario 3: No rapid true polar wander between 810 and 780 Ma? (a) In scenario 3, we compare the overall mean ca. 810 Ma poles derived in scenario 1 (red) and scenario 2 (green) with the 780 Ma (LT1) pole (purple). The angular distance between the 810 and 780 Ma poles is  $\sim 53^\circ$ , implying an APW rate of  $\sim 1.8^\circ/\text{Myr}$ , which is within estimated rates of conventional TPW ( $< 2.0^\circ/\text{Myr}$ ) for the past 540 Ma (Torsvik et al., 2012). However, the difference between the poles is mostly in the declination (rotational) component (small circle drawn about the Scenario 1 pole, shown in blue), suggesting that a vertical axis rotation could account for most of the apparent pole motion. Therefore, evidence for TPW between 810 and 780 Ma is tenuous, and can likely be explained by deformation producing vertical axis block rotation in the Phanerozoic, and/or regional remagnetization in the mid-Paleozoic. (b) An inclination-only fold test for the remaining Tonian poles after Scenario 2 (excluding three poles suspected of remagnetization) yields  $\kappa_{max}$  at 102 % unfolding.

735 and 780 Ma is tenuous, and can be explained by a regional mid-Paleozoic remagnetiza-  
736 tion and/or vertical axis rotations in the Phanerozoic.

### 737 5.3 Summary of discussion

738 We show that rapid pole variations postulated for ca. 805 Ma can be explained by  
739 vertical axis rotations and/or regional remagnetization in South China, without invok-  
740 ing extreme plate motion, rapid TPW or abnormal field geometry. Tonian (820-800 Ma)  
741 poles for the SCB are distributed along a small circle centered on the mean site location  
742 and can be brought into close alignment if vertical axis rotations are permitted. How-  
743 ever, some poles derived from Tonian-ages rocks lie within a cluster of Ordovician poles  
744 (when plotted in the same hemisphere), leading us to conclude that paleomagnetic data  
745 from other Madiyi-equivalent formations may reflect a regional overprint, not primary  
746 remanences. A complicated mixture of primary and secondary magnetizations may have  
747 led some studies to support a rapid TPW (or ITPW) event. Similarity between South  
748 China's Tonian and Ordovician paleolatitudes could be contributing to the confusion,  
749 if an Ordovician remagnetization is widespread. We think that paleomagnetic directions  
750 used in favour of rapid TPW are instead artefacts of the complicated remanence acqui-  
751 sition process where DRM is partially or fully obscured by a CRM.

752 Our results call for careful consideration of paleomagnetic signals in sedimentary  
753 sequences containing diverse lithologies, particularly those with hematite-bearing (red)  
754 mudstones and sandstones. Further work is needed to unravel the response of the Yangtze  
755 craton to the Wuyi-Yunkai Orogeny and understand mechanisms for remagnetization of  
756 pre-Silurian strata. If the discordant poles are indeed artefacts of a tectono-thermal event  
757 in the Ordovician, then any proposed remagnetization mechanism must be capable of  
758 resetting or overprinting paleomagnetic signals across a range of lithologies and magnetic  
759 mineralogies, as is also true for the Cretaceous overprint component.

## 760 6 Conclusions

761 The Laoshanya Formation in Yangjiaping contains a complicated paleomagnetic  
762 record which offers a unique opportunity to investigate remanence acquisition processes  
763 in hematite-bearing sedimentary rocks. Remarkably, the red beds seem to have preserved  
764 a primary (depositional) Tonian signal (component C), as well as secondary magneti-  
765 zations residing in hematite created or reset in the Ordovician (B) and Cretaceous (A).  
766 From our study we conclude the following:

- 767 1. Stepwise thermal demagnetization of 1188 samples isolated three end-member mag-  
768 netization components (A-C) that combine in a complex and out-of-sequence man-  
769 ner throughout the 85 m of sampled section. Vector unmixing identifies the pro-  
770 portions of the three components, which are distinguished by their rock magnetic  
771 characteristics and microscopy, and may respectively represent the most common  
772 hematite phases found in red beds: detrital specular grains, intergranular authi-  
773 genic grains, and pigmentary coatings (Q. R. Zhang & Piper, 1997). Component  
774 C is carried mostly by coarse grained hematite and is interpreted to be a primary  
775 remanence based on a positive reversal test. Components A and B are carried by  
776 single domain-sized hematite and are interpreted as overprint components.
- 777 2. High-precision U-Pb dating of zircons extracted from two tuff horizons in the sec-  
778 tion yielded dates of  $807.52 \pm 0.18/0.27/0.91$  Ma and  $804.50 \pm 0.22/0.30/0.91$  Ma,  
779 which constrain the depositional age of the section between 809 and 804 Ma (us-  
780 ing linear extrapolation). The primary nature of Component C is further supported  
781 by its agreement with some coeval poles from South China. Our new pole sup-  
782 ports a stable, high-latitude position for the SCB between 809 and 804 Ma, and  
783 therefore a peripheral location with respect to the Rodinian supercontinent.

- 784 3. Component B is found mostly in fine-grained beds and likely formed authigeni-  
785 cally at temperatures up to 260°C in Yangjiaping, and up to 360°C in Tonian-aged  
786 red beds farther south. In the Laoshanya Formation, the component resides in fine  
787 idiomorphic hematite crystals (1–2 μm) and/or in dense clusters/pseudomorphs  
788 of microplaty hematite. The corresponding pole lies close to several Ordovician  
789 poles from the SCB, suggesting that the age of magnetic acquisition is Ordovician.  
790 We link component B to a regional low-grade tectono-thermal (< 260°C) event  
791 in the Late Ordovician, which may have partially or fully remagnetized pre-Silurian  
792 formations on the Yangtze craton.
- 793 4. Component A is an overprint acquired during the Cretaceous normal superchron,  
794 a common direction found throughout South China. Thermal remanence curves  
795 for this component are consistent with fine-grained or pigmentary hematite, as-  
796 sumed to have formed by the oxidation of Fe-rich minerals. This interpretation  
797 is consistent with rock magnetic experiments and microscopic observations of abun-  
798 dant (< 1 μm) hematite flakes and needles in all specimens.

## 799 Acknowledgments

800 This work was supported by the German Research Foundation (DFG grant GI712/18-  
801 1), the LMU-China Academic Network (LMU-ChAN), the National Natural Science Foun-  
802 dation of China (no. 41874076 and no. 41888101), and a Swiss Government Excellence  
803 Scholarship. We thank Yuyang Hu, Zhaoyang Zhou and Junjie Xu for their assistance  
804 in the field. We thank Leon Kaub, Petter Silkoset, Claudia Trepmann, Uwe Kirscher,  
805 Erwin Appel, Maria Ovtcharova, Aurélia Crinière, Sophie Nowak and Imène Esteve for  
806 assistance in their respective laboratories. We thank Ann Hirt for useful discussions and  
807 Yuchen Chi for assistance with translations and geological maps. SG expresses deep grat-  
808 itude to Qirui Zhang for introducing him to the Yangjiaping Section in 1990 and to his  
809 family for moral sustenance.

## 810 Author contributions

811 BR and SG jointly conceived of the idea for this project and wrote the funding pro-  
812 posal together. JT, BR, EM, MW, SG and XZ carried out initial fieldwork in 2019. JM  
813 carried out supplementary sampling in 2021. JT was responsible for paleomagnetic and  
814 rock magnetic measurements with significant input from SG. EM, FD and JT were jointly  
815 responsible for the microscopic observations and mineralogical analyses. JT and AP car-  
816 ried out sample preparation and U-Pb geochronology with supervision by US. JT wrote  
817 the manuscript with significant input from BR and SG, and in consultation with the other  
818 authors. All authors have read and approved the final manuscript.

## 819 Availability statement

820 Paleomagnetic data are available in the MagIC database and all other data are avail-  
821 able on GitHub [links to be provided upon acceptance of this paper].

## 822 References

- 823 Alken, P., Thébault, E., Beggan, C. D., Amit, H., Aubert, J., Baerenzung, J.,  
824 ... Zhou, B. (2021). International Geomagnetic Reference Field: the  
825 thirteenth generation. *Earth, Planets and Space*, 73(1). doi: 10.1186/  
826 s40623-020-01288-x
- 827 Bai, L., Zhu, R., Wu, H., Guo, B., & Lü, J. (1998). New Cambrian paleomag-  
828 netic pole for Yangtze Block. *Science in China, Series D: Earth Sciences*,  
829 41(SUPPL.), 70–71. doi: 10.1360/yd1998-41-S2-66

- 830 Basu, A., & Molinaroli, E. (1989). Provenance characteristics of detrital opaque Fe-  
831 Ti oxide minerals. *Journal of Sedimentary Petrology*, *59*(6), 922–934. doi: 10  
832 .1306/212F90B6-2B24-11D7-8648000102C1865D
- 833 Blaauw, M., & Christeny, J. A. (2011). Flexible paleoclimate age-depth models us-  
834 ing an autoregressive gamma process. *Bayesian Analysis*, *6*(3), 457–474. doi:  
835 10.1214/11-BA618
- 836 Butler, R. F. (1992). *Paleomagnetism: Magnetic domains to geologic terranes*.  
837 Boston: Blackwell.
- 838 Cawood, P. A., Wang, W., Zhao, T., Xu, Y., Mulder, J. A., Pisarevsky, S. A., ...  
839 Zi, J. W. (2020). Deconstructing South China and consequences for recon-  
840 structing Nuna and Rodinia. *Earth-Science Reviews*, *204* (November 2019),  
841 103169. doi: 10.1016/j.earscirev.2020.103169
- 842 Cawood, P. A., Wang, Y., Xu, Y., & Zhao, G. (2013). Locating South China in Ro-  
843 dinia and Gondwana: A fragment of greater India lithosphere? *Geology*, *41*(8),  
844 903–906. doi: 10.1130/G34395.1
- 845 Cawood, P. A., Zhao, G., Yao, J., Wang, W., Xu, Y., & Wang, Y. (2018). Re-  
846 constructing South China in Phanerozoic and Precambrian superconti-  
847 nents. *Earth-Science Reviews*, *186* (January), 173–194. doi: 10.1016/  
848 j.earscirev.2017.06.001
- 849 Chang, L., Zhang, S., Li, H., Xian, H., Wu, H., & Yang, T. (2022). New paleomag-  
850 netic insights into the Neoproterozoic connection between South China and  
851 India and their position in Rodinia. *Geophysical Research Letters*, *49*(10). doi:  
852 10.1029/2022GL098348
- 853 Charvet, J. (2013). The Neoproterozoic-Early Paleozoic tectonic evolution of the  
854 South China Block: An overview. *Journal of Asian Earth Sciences*, *74*, 198–  
855 209. doi: 10.1016/j.jseaes.2013.02.015
- 856 Chen, X., Fan, J. X., Chen, Q., Tang, L., & Hou, X. D. (2014). Toward a stepwise  
857 Kwangsi Orogeny. *Science China Earth Sciences*, *57*(3), 379–387. doi: 10  
858 .1007/s11430-013-4815-y
- 859 Collinson, D. W. (1974). The role of pigment and specularite in the remanent mag-  
860 netism of red sandstones. *Geophysical Journal of the Royal Astronomical Soci-  
861 ety*, *38*(2), 253–264. doi: 10.1111/j.1365-246X.1974.tb04119.x
- 862 Condon, D. J., Schoene, B., McLean, N. M., Bowring, S. A., & Parrish, R. R.  
863 (2015). Metrology and traceability of U-Pb isotope dilution geochronology  
864 (EARTHTIME Tracer Calibration Part I). *Geochimica et Cosmochimica Acta*,  
865 *164*, 464–480. doi: 10.1016/j.gca.2015.05.026
- 866 Dekkers, M. J., & Linssen, J. H. (1989). Rockmagnetic properties of fine-grained  
867 natural low-temperature haematite with reference to remanence acquisition  
868 mechanisms in red beds. *Geophysical Journal International*, *99*(1), 1–18. doi:  
869 10.1111/j.1365-246X.1989.tb02012.x
- 870 Driscoll, P. E. (2016). Simulating 2 Ga of geodynamo history. *Geophysical Research  
871 Letters*, *43*(11), 5680–5687. doi: 10.1002/2016GL068858
- 872 Dunlop, D. J. (1974). Thermal enhancement of magnetic susceptibility. *Journal of  
873 Geophysics*, *40*(1), 439–451.
- 874 Edward, O., Paul, A. N., Bucher, H., Vérard, C., Adatte, T., Sonke, J. E., ... Ven-  
875 nemann, T. (2023). Timing and Provenance of Volcanic Fluxes Around the  
876 Permian-Triassic Boundary Mass Extinction in South China: U-Pb Zircon  
877 Geochronology, Volcanic Ash Geochemistry and Mercury Isotopes. *Geochem-  
878 istry, Geophysics, Geosystems*, *24*(6). doi: 10.1029/2023GC010912
- 879 Enkin, R. J., & Watson, G. S. (1996). Statistical analysis of palaeomagnetic inclina-  
880 tion data. *Geophysical Journal International*, *126*(2), 495–504. doi: 10.1111/  
881 j.1365-246X.1996.tb05305.x
- 882 Evans, D. A. (2002). True polar wander and supercontinents. *Tectonophysics*, *362*,  
883 303–320. doi: 10.1016/s0040-1951(02)00642-x
- 884 Evans, D. A. (2021). Meso-Neoproterozoic Rodinia supercycle. *Ancient Super-*

- 885 *continents and the Paleogeography of Earth*, 549–576. doi: 10.1016/b978-0-12  
886 -818533-9.00006-0
- 887 Evans, D. A., Li, Z. X., Kirschvink, J. L., & Wingate, M. T. (2000). A high-quality  
888 mid-Neoproterozoic paleomagnetic pole from South China, with implications  
889 for ice ages and the breakup configuration of Rodinia. *Precambrian Research*,  
890 *100*(1-3), 313–334. doi: 10.1016/S0301-9268(99)00079-0
- 891 Evans, D. A., Li, Z. X., & Murphy, J. B. (2016). Four-dimensional context of  
892 Earth’s supercontinents. In Z. X. Li, D. A. D. Evans, & J. B. Murphy (Eds.),  
893 *Supercontinent cycles through earth history* (Vol. 424, pp. 1–14). The Geologi-  
894 cal Society of London. doi: 10.1144/SP424.12
- 895 Eyster, A., Weiss, B. P., Karlstrom, K., & Macdonald, F. A. (2020). Paleomag-  
896 netism of the Chuar Group and evaluation of the late Tonian Laurentian  
897 apparent polar wander path with implications for the makeup and breakup of  
898 Rodinia. *Bulletin of the Geological Society of America*, *132*(3-4), 710–738. doi:  
899 10.1130/B32012.1
- 900 Fang, W., Voo, R. V. D., & Liang, Q. (1990). Ordovician Paleomagnetism of East-  
901 ern Yunnan, China. *Geophysical Research Letters*, *17*(7), 953–956.
- 902 Fisher, R. (1953). Dispersion on a sphere. *Proceedings of the Royal Society*, *217*,  
903 295–305. doi: 10.1098/rspa.1953.0064
- 904 Flinn, D. (1962). On folding during three-dimensional progressive deformation.  
905 *Quarterly Journal of the Geological Society*, *118*(1-4), 385–428. doi: 10.1144/  
906 gsjgs.118.1.0385
- 907 Gao, L., Yang, Z., Han, Z., Tong, Y., Jing, X., & Zhang, S. H. (2018). Remag-  
908 netization of the Lower Ordovician Hongshiya Formation of the southwest-  
909 ern Yangtze Block. *Tectonophysics*, *738-739*(December 2017), 83–91. doi:  
910 10.1016/j.tecto.2018.05.017
- 911 Gerstenberger, H., & Haase, G. (1997). A highly effective emitter substance for  
912 mass spectrometric Pb isotope ratio determinations. *Chemical Geology*, *136*(3-  
913 4), 309–312. doi: 10.1016/S0009-2541(96)00033-2
- 914 Gilder, S. A., & Courtillot, V. (1997). Timing of the North-South China collision  
915 from new middle to late Mesozoic paleomagnetic data from the North China  
916 Block. *Journal of Geophysical Research: Solid Earth*, *102*(B8), 17713–17727.  
917 doi: 10.1029/97jb01201
- 918 Gilder, S. A., Leloup, P. H., Courtillot, V., Chen, Y., Coe, R. S., Zhao, X., ... Zhu,  
919 R. (1999). Tectonic evolution of the Tancheng-Lujiang (Tan-Lu) fault via  
920 Middle Triassic to Early Cenozoic paleomagnetic data. *Journal of Geophys-  
921 ical Research: Solid Earth*, *104*(B7), 15365–15390. Retrieved from [http://](http://doi.wiley.com/10.1029/1999JB900123)  
922 [doi.wiley.com/10.1029/1999JB900123](http://doi.wiley.com/10.1029/1999JB900123) doi: 10.1029/1999JB900123
- 923 Gilder, S. A., Tan, X., Bucher, H., Kuang, G., & Yin, J. (2008). Optimization of ap-  
924 parent polar wander paths: An example from the South China plate. *Physics  
925 of the Earth and Planetary Interiors*, *169*(1-4), 166–177. doi: 10.1016/j.pepi  
926 .2008.07.016
- 927 Halverson, G. P., Shen, C., Davies, J. H., & Wu, L. (2022). A Bayesian ap-  
928 proach to inferring depositional ages applied to a late Tonian reference  
929 section in Svalbard. *Frontiers in Earth Science*, *10*(February). doi:  
930 10.3389/feart.2022.798739
- 931 Han, Z., Yang, Z., Tong, Y., & Jing, X. (2015). New paleomagnetic results from  
932 Late Ordovician rocks of the Yangtze Block, South China, and their paleo-geo-  
933 graphic implications. *Journal of Geophysical Research: Solid Earth*, *120*(7),  
934 4759–4772. doi: 10.1002/2015JB012005
- 935 Hoffman, P. F., Kaufman, A. J., Halverson, G. P., & Schrag, D. P. (1998). A neo-  
936 proterozoic snowball earth. *Science*, *281*(5381), 1342–1346. doi: 10.1126/  
937 science.281.5381.1342
- 938 Hounslow, M. W., Domeier, M., & Biggin, A. J. (2018). Subduction flux modulates  
939 the geomagnetic polarity reversal rate. *Tectonophysics*, *742-743*, 34–49. doi: 10

- .1016/j.tecto.2018.05.018
- 940  
941 Huang, B., Yan, Y., Piper, J. D., Zhang, D., Yi, Z., Yu, S., & Zhou, T. (2018). Pa-  
942 leomagnetic constraints on the paleogeography of the East Asian blocks during  
943 Late Paleozoic and Early Mesozoic times. *Earth-Science Reviews*, *186*(5),  
944 8–36. doi: 10.1016/j.earscirev.2018.02.004
- 945 Huang, K., Opdyke, N. D., & Zhu, R. (2000). Further paleomagnetic results from  
946 the Silurian of the Yangtze Block and their implications. *Earth and Planetary  
947 Science Letters*, *175*(3-4), 191–202. doi: 10.1016/S0012-821X(99)00302-7
- 948 Jiang, X. S., Wang, J., Cui, X. Z., Zhuo, J. W., Xiong, G. Q., Lu, J. Z., & Liu,  
949 J. H. (2012). Zircon SHRIMP U-Pb geochronology of the Neoproterozoic  
950 Chengjiang Formation in central Yunnan Province (SW China) and its geo-  
951 logical significance. *Science China Earth Sciences*, *55*(11), 1815–1826. doi:  
952 10.1007/s11430-012-4530-0
- 953 Jing, X., Evans, D. A., Yang, Z., Tong, Y., Xu, Y., & Wang, H. (2021). Inverted  
954 South China: A novel configuration for Rodinia and its breakup. *Geology*,  
955 *49*(4), 463–467. doi: 10.1130/G47807.1
- 956 Jing, X., Yang, Z., Evans, D. A., Tong, Y., Xu, Y., & Wang, H. (2020). A pan-  
957 latitudinal Rodinia in the Tonian true polar wander frame. *Earth and Plane-  
958 tary Science Letters*, *530*, 115880. doi: 10.1016/j.epsl.2019.115880
- 959 Jing, X., Yang, Z., Tong, Y., & Han, Z. (2015). A revised paleomagnetic pole  
960 from the mid-Neoproterozoic Liantuo Formation in the Yangtze block and  
961 its paleogeographic implications. *Precambrian Research*, *268*, 194–211. doi:  
962 10.1016/j.precamres.2015.07.007
- 963 Kent, D. V., Zeng, X., Zhang Wen, Y., & Opdyke, N. D. (1987). Widespread  
964 late Mesozoic to recent remagnetization of Paleozoic and lower Triassic sed-  
965 imentary rocks from South China. *Tectonophysics*, *139*(1-2), 133–143. doi:  
966 10.1016/0040-1951(87)90202-2
- 967 Kirschvink, J. L. (1980). The least-squares line and plane and the analysis of palaeo-  
968 magnetic data. *Geophysical Journal of the Royal Astronomical Society*, *62*(3),  
969 699–718. doi: 10.1111/j.1365-246X.1980.tb02601.x
- 970 Kirschvink, J. L., Ripperdan, R. L., & Evans, D. A. (1997). Evidence for a  
971 large-scale reorganization of Early Cambrian continental masses by iner-  
972 tial interchange true polar wander. *Science*, *277*(5325), 541–545. doi:  
973 10.1126/science.277.5325.541
- 974 Kletetschka, G., & Wasilewski, P. J. (2002). Grain size limit for SD hematite.  
975 *Physics of the Earth and Planetary Interiors*, *129*(1-2), 173–179. doi:  
976 10.1016/S0031-9201(01)00271-0
- 977 Kodama, K. P. (2012). *Paleomagnetism of Sedimentary Rocks: Process and Interpre-  
978 tation*. John Wiley and Sons. doi: 10.1002/9781118384138
- 979 Kodama, K. P. (2013). Grand challenges in geomagnetism and paleomagnetism.  
980 *Frontiers in Earth Science*, *1*(Dec), 1–3. doi: 10.3389/feart.2013.00003
- 981 Lan, Z., Li, X. H., Zhu, M., Zhang, Q., & Li, Q. L. (2015). Revisiting the Liantuo  
982 Formation in Yangtze Block, South China: SIMS U-Pb zircon age constraints  
983 and regional and global significance. *Precambrian Research*, *263*(November  
984 2018), 123–141. doi: 10.1016/j.precamres.2015.03.012
- 985 Li, C., Wang, X., He, C., Wu, X., Kong, Z., & Li, X. (2017). China National Digi-  
986 tal Geological Map (Public Version at 1:200000 Scale) Spatial Database. *Geol-  
987 ogy in China*, *46*, 1–14. doi: 10.23650/data.A.2019.NGA120157.K1.1.1.V1
- 988 Li, D., Yang, Z., Liu, Y., Yang, K., Wu, D., & Cai, P. (2022). Timing and proven-  
989 nance transition of the Neoproterozoic Wuling Unconformity and Xihuangshan  
990 Unconformity of the Yangtze Block: Responses to peripheral orogenic Events.  
991 *Minerals*, *12*(5), 1–27. doi: 10.3390/min12050596
- 992 Li, S., Cao, J., Feng, Z., Liu, X., Qin, Y., Hu, R., & Wang, C. (2022). Neopro-  
993 terozoic to Palaeozoic tectonic deformation history of the western Jiang-  
994 nan Orogen, South China: Insights from new structural and geochronologi-

- cal data from northern Guangxi. *Geological Journal*, 57(1), 292–316. doi: 10.1002/gj.4298
- Li, Z. X., Bogdanova, S. V., Collins, A. S., Davidson, A., De Waele, B., Ernst, R. E., ... Vernikovsky, V. (2008). Assembly, configuration, and break-up history of Rodinia: A synthesis. *Precambrian Research*, 160(1-2), 179–210. doi: 10.1016/j.precamres.2007.04.021
- Li, Z. X., Evans, D. A., & Halverson, G. P. (2013). Neoproterozoic glaciations in a revised global palaeogeography from the breakup of Rodinia to the assembly of Gondwanaland. *Sedimentary Geology*, 294, 219–232. doi: 10.1016/j.sedgeo.2013.05.016
- Li, Z. X., Evans, D. A., & Zhang, S. (2004). A 90° spin on Rodinia: Possible causal links between the Neoproterozoic supercontinent, superplume, true polar wander and low-latitude glaciation. *Earth and Planetary Science Letters*, 220(3-4), 409–421. doi: 10.1016/S0012-821X(04)00064-0
- Li, Z. X., Li, X. H., Wartho, J. A., Clark, C., Li, W. X., Zhang, C. L., & Bao, C. (2010). Magmatic and metamorphic events during the early Paleozoic Wuyi-Yunkai orogeny, southeastern South China: New age constraints and pressure-temperature conditions. *Bulletin of the Geological Society of America*, 122(5-6), 772–793. doi: 10.1130/B30021.1
- Ma, G., Li, H., & Zhang, Z. (1984). An investigation of the age limits of the Sinian System in South China [in Chinese with English abstract]. *Bulletin of Yichang Institute of Geology and Mineral Resources*, 8, 1–29.
- Macouin, M., Ader, M., Moreau, M. G., Poitou, C., Yang, Z., & Sun, Z. (2012). Deciphering the impact of diagenesis overprint on negative  $\delta^{13}\text{C}$  excursions using rock magnetism: Case study of Ediacaran carbonates, Yangjiaping section, South China. *Earth and Planetary Science Letters*, 351-352, 281–294. doi: 10.1016/j.epsl.2012.06.057
- Macouin, M., Besse, J., Ader, M., Gilder, S. A., Yang, Z., Sun, Z., & Agrinier, P. (2004). Combined paleomagnetic and isotopic data from the Doushan-tuo carbonates, South China: Implications for the "snowball Earth" hypothesis. *Earth and Planetary Science Letters*, 224(3-4), 387–398. doi: 10.1016/j.epsl.2004.05.015
- Maloof, A. C., Halverson, G. P., Kirschvink, J. L., Schrag, D. P., Weiss, B. P., & Hoffman, P. F. (2006). Combined paleomagnetic, isotopic, and stratigraphic evidence for true polar wander from the Neoproterozoic Akademikerbreen Group, Svalbard, Norway. *Bulletin of the Geological Society of America*, 118(9-10), 1099–1124. doi: 10.1130/B25892.1
- Marshall, C. R. (2006). Explaining the Cambrian "explosion" of animals. *Annual Review of Earth and Planetary Sciences*, 34, 355–384. doi: 10.1146/annurev.earth.33.031504.103001
- McElhinny, M. W. (1964). Statistical significance of the fold test in paleomagnetism. *Geophysical Journal of the Royal Astronomical Society*, 8, 338–340. doi: 10.1111/j.1365-246X.1964.tb06300.x
- McFadden, P. L., & McElhinny, M. W. (1990). Classification of the reversal test in palaeomagnetism. *Geophysical Journal International*, 103(3), 725–729. doi: 10.1111/j.1365-246X.1990.tb05683.x
- McLean, N. M., Condon, D. J., Schoene, B., & Bowring, S. A. (2015). Evaluating uncertainties in the calibration of isotopic reference materials and multi-element isotopic tracers (EARTHTIME Tracer Calibration Part II). *Geochimica et Cosmochimica Acta*, 164, 481–501. doi: 10.1016/j.gca.2015.02.040
- Meert, J. G., Levashova, N. M., Bazhenov, M. L., & Landing, E. (2016). Rapid changes of magnetic Field polarity in the late Ediacaran: Linking the Cambrian evolutionary radiation and increased UV-B radiation. *Gondwana Research*, 34, 149–157. doi: 10.1016/j.gr.2016.01.001
- Meert, J. G., Pivarunas, A. F., Evans, D. A., Pisarevsky, S. A., Pesonen, L. J., Li,

- 1050 Z. X., ... Salminen, J. M. (2020). The magnificent seven: A proposal for  
 1051 modest revision of the Van der Voo (1990) quality index. *Tectonophysics*,  
 1052 *790*(March), 228549. doi: 10.1016/j.tecto.2020.228549
- 1053 Meng, J., Gilder, S. A., Li, Y., Chen, Y., Zhang, C., Zhou, Z., ... Wang, C. (2022).  
 1054 Remagnetization age and mechanism of Cretaceous sediments in relation to  
 1055 dyke intrusion, Hainan Island: Tectonic implications for South China and the  
 1056 Red River Fault. *Journal of Geophysical Research: Solid Earth*, *127*(1), 1–19.  
 1057 doi: 10.1029/2021JB023474
- 1058 Niu, J., Li, Z. X., & Zhu, W. (2016). Palaeomagnetism and geochronology of mid-  
 1059 Neoproterozoic Yanbian dykes, South China: Implications for a c. 820-800 Ma  
 1060 true polar wander event and the reconstruction of Rodinia. *Geological Society*  
 1061 *Special Publication*, *424*(1), 192–211. doi: 10.1144/SP424.11
- 1062 Ogg, J. G. (2012). Geomagnetic Polarity Time Scale. *The Geologic Time Scale*  
 1063 *2012*, 1-2, 85–113. doi: 10.1016/B978-0-444-59425-9.00005-6
- 1064 Opdyke, N. D., Huang, K., Xu, G., Zhang, W., & Kent, D. (1987). Paleomagnetic  
 1065 results from the Silurian of the Yangtze paraplatform. *Tectonophysics*, *139*(1-  
 1066 2), 123–132. doi: 10.1016/0040-1951(87)90201-0
- 1067 O'Reilly, W. (1984). Magnetic properties of other mineral systems. In *Rock*  
 1068 *and mineral magnetism* (pp. 172–193). Boston, MA: Springer US. Retrieved  
 1069 from [http://link.springer.com/10.1007/978-1-4684-8468-7\\_{\\\_}8](http://link.springer.com/10.1007/978-1-4684-8468-7_{\_}8) doi:  
 1070 10.1007/978-1-4684-8468-7\_8
- 1071 Özdemir, Ö., & Dunlop, D. J. (2002). Thermoremanence and stable memory of  
 1072 single-domain hematites. *Geophysical Research Letters*, *29*(18), 10–13. doi: 10  
 1073 .1029/2002GL015597
- 1074 Özdemir, Ö., & Dunlop, D. J. (2005). Thermoremanent magnetization of multidomain  
 1075 hematite. *Journal of Geophysical Research*, *110*(B09104), 1–8. doi: 10  
 1076 .1029/2005JB003820
- 1077 Özdemir, Ö., & Dunlop, D. J. (2014). Hysteresis and coercivity of hematite.  
 1078 *Journal of Geophysical Research: Solid Earth*, *119*(4), 2582–2594. doi:  
 1079 10.1002/2013JB010739
- 1080 Özdemir, Ö., Dunlop, D. J., & Berquó, T. S. (2008). Morin transition in hematite:  
 1081 Size dependence and thermal hysteresis. *Geochemistry, Geophysics, Geosys-*  
 1082 *tems*, *9*(10). doi: 10.1029/2008GC002110
- 1083 Park, Y., Swanson-Hysell, N. L., Xian, H., Zhang, S., Condon, D. J., Fu, H., & Mac-  
 1084 donald, F. A. (2021). A Consistently High-Latitude South China From 820  
 1085 to 780 Ma: Implications for Exclusion From Rodinia and the Feasibility of  
 1086 Large-Scale True Polar Wander. *Journal of Geophysical Research: Solid Earth*,  
 1087 *126*(6), 1–29. doi: 10.1029/2020JB021541
- 1088 Parry, W. T., Chan, M. A., & Beitler, B. (2004). Chemical bleaching indicates  
 1089 episodes of fluid flow in deformation bands in sandstone. *American Association*  
 1090 *of Petroleum Geologists Bulletin*, *88*(2), 175–191. doi: 10.1306/09090303034
- 1091 Raub, T. D., Kirschvink, J. L., & Evans, D. A. (2015). True Polar Wander:  
 1092 Linking Deep and Shallow Geodynamics to Hydro- and Biospheric Hy-  
 1093 potheses. *Treatise on Geophysics: Second Edition*, *5*(1969), 511–530. doi:  
 1094 10.1016/B978-0-444-53802-4.00108-1
- 1095 Roberts, A. P., Yulong Cui, & Verosub, K. L. (1995). *Wasp-waisted hysteresis loops:*  
 1096 *mineral magnetic characteristics and discrimination of components in mixed*  
 1097 *magnetic systems* (Vol. 100) (No. B9). doi: 10.1029/95jb00672
- 1098 Roberts, N. M. (2013). The boring billion? - Lid tectonics, continental growth  
 1099 and environmental change associated with the Columbia supercontinent. *Geo-*  
 1100 *science Frontiers*, *4*(6), 681–691. doi: 10.1016/j.gsf.2013.05.004
- 1101 Rochette, P., Mathé, P. E., Esteban, L., Rakoto, H., Bouchez, J. L., Liu, Q., &  
 1102 Torrent, J. (2005). Non-saturation of the defect moment of goethite and fine-  
 1103 grained hematite up to 57 Teslas. *Geophysical Research Letters*, *32*(22), 1–4.  
 1104 doi: 10.1029/2005GL024196

- 1105 Sadler, P. M. (1981). Sediment accumulation rates and the completeness of  
 1106 stratigraphic sections. *The Journal of Geology*, *89*(5), 569–584. doi:  
 1107 10.1086/628623
- 1108 Saint-Bezar, B., Hebert, R. L., Aubourg, C., Robion, P., Swennen, R., & Frizon  
 1109 De Lamotte, D. (2002). Magnetic fabric and petrographic investigation of  
 1110 hematite-bearing sandstones within ramp-related folds: Examples from the  
 1111 South Atlas Front (Morocco). *Journal of Structural Geology*, *24*(9), 1507–1520.  
 1112 doi: 10.1016/S0191-8141(01)00140-7
- 1113 Schaltegger, U., Ovtcharova, M., Gaynor, S. P., Schoene, B., Wotzlaw, J. F., Davies,  
 1114 J. F., ... Chelle-Michou, C. (2021). Long-term repeatability and interlabora-  
 1115 tory reproducibility of high-precision ID-TIMS U-Pb geochronology. *Journal of*  
 1116 *Analytical Atomic Spectrometry*, *36*(7), 1466–1477. doi: 10.1039/d1ja00116g
- 1117 Schaltegger, U., Schmitt, A. K., & Horstwood, A. (2015). U-Th-Pb zircon  
 1118 geochronology by ID-TIMS, SIMS, and laser. *Chemical Geology*, *402*(8),  
 1119 89–110.
- 1120 Schmitz, B., Bergström, S. M., & Xiaofeng, W. (2010). The middle Darriwil-  
 1121 ian (Ordovician)  $\delta^{13}\text{C}$  excursion (MDICE) discovered in the Yangtze Plat-  
 1122 form succession in China: Implications of its first recorded occurrences out-  
 1123 side Baltoscandia. *Journal of the Geological Society*, *167*(2), 249–259. doi:  
 1124 10.1144/0016-76492009-080
- 1125 Schoene, B., Crowley, J. L., Condon, D. J., Schmitz, M. D., & Bowring, S. A.  
 1126 (2006). Reassessing the uranium decay constants for geochronology using  
 1127 ID-TIMS U-Pb data. *Geochimica et Cosmochimica Acta*, *70*(2), 426–445. doi:  
 1128 10.1016/j.gca.2005.09.007
- 1129 Song, G., Wang, X., Shi, X., & Jiang, G. (2017). New U-Pb age constraints on the  
 1130 upper Banxi Group and synchrony of the Sturtian glaciation in South China.  
 1131 *Geoscience Frontiers*, *8*(5), 1161–1173. doi: 10.1016/j.gsf.2016.11.012
- 1132 Sprain, C. J., Feinberg, J. M., Renne, P. R., & Jackson, M. (2016). Importance  
 1133 of titanohematite in detrital remanent magnetizations of strata spanning the  
 1134 Cretaceous-Paleogene boundary, Hell Creek region, Montana. *Geochemistry,*  
 1135 *Geophysics, Geosystems*, *17*(3), 660–678. doi: 10.1002/2015GC006191
- 1136 Sun, H.-Q., Huang, J.-Z., Guo, L.-Q., & Chen, J. (2012). Subdivision and isotopic  
 1137 age of Lengjiaxi Group in Hunan Province. *Geology and Mineral Resources of*  
 1138 *South China*, *28*(1), 20–26.
- 1139 Swanson-Hysell, N. L., Maloof, A. C., Kirschvink, J. L., Evans, D. A., Halverson,  
 1140 G. P., & Hurtgen, M. T. (2012). Constraints on neoproterozoic paleogeogra-  
 1141 phy and paleozoic orogenesis from paleomagnetic records of the bitter springs  
 1142 formation, amadeus basin, central Australia. *American Journal of Science*,  
 1143 *312*(8), 817–884. doi: 10.2475/08.2012.01
- 1144 Tan, X., Kodama, K. P., Gilder, S. A., Courtillot, V., & Cogné, J. P. (2007). Palaeo-  
 1145 magnetic evidence and tectonic origin of clockwise rotations in the Yangtze  
 1146 fold belt, South China Block. *Geophysical Journal International*, *168*(1),  
 1147 48–58. doi: 10.1111/j.1365-246X.2006.03195.x
- 1148 Tauxe, L., & Kent, D. V. (2004). A simplified statistical model for the geomagnetic  
 1149 field and the detection of shallow bias in paleomagnetic inclinations: Was the  
 1150 ancient magnetic field dipolar? *Geophysical Monograph Series*, *145*, 101–115.  
 1151 doi: 10.1029/145GM08
- 1152 Till, J. L., Guyodo, Y., Lacroix, F., Morin, G., & Ona-Nguema, G. (2015). Goethite  
 1153 as a potential source of magnetic nanoparticles in sediments. *Geology*, *43*(1),  
 1154 75–78. doi: 10.1130/G36186.1
- 1155 Tonti-Filippini, J. A. D., & Gilder, S. A. (2023). Vector unmixing of multicom-  
 1156 ponent palaeomagnetic data. *Geophysical Journal International*, *233*(3), 1632–  
 1157 1654. doi: 10.1093/gji/ggac505
- 1158 Torsvik, T. H. (2003). The Rodinia jigsaw puzzle. *Science*, *300*(5624), 1379–1381.  
 1159 doi: 10.1126/science.1083469

- 1160 Torsvik, T. H., Van der Voo, R., Preeden, U., Mac Niocaill, C., Steinberger, B.,  
 1161 Doubrovine, P. V., ... Cocks, L. R. M. (2012). Phanerozoic Polar Wander,  
 1162 Palaeogeography and Dynamics. *Earth-Science Reviews*, 114(3-4), 325–368.  
 1163 doi: 10.1016/j.earscirev.2012.06.007
- 1164 Volk, M. W. R. (2016). *Influence of pressure, temperature and composition on mag-*  
 1165 *netic recording in meteorites* (Doctoral dissertation). doi: 10.5282/edoc.19824
- 1166 Wack, M. R. (2023). Improved anisotropy of magnetic remanence results from vec-  
 1167 torial readings using novel refinement method. *Geophysical Journal Interna-*  
 1168 *tional*, 233(2), 1113–1123. doi: 10.1093/gji/ggac500
- 1169 Wack, M. R., & Gilder, S. A. (2012). The SushiBar: An automated system for pa-  
 1170 leomagnetic investigations. *Geochemistry, Geophysics, Geosystems*, 13(12), 1–  
 1171 24. doi: 10.1029/2011GC003985
- 1172 Walker, T. R., Larson, E. E., & Hoblitt, R. P. (1981). Nature and origin of hematite  
 1173 in the Moenkopi Formation (Triassic), Colorado Plateau: A contribution to  
 1174 the origin of magnetism in red beds. *Journal of Geophysical Research*, 86(B1),  
 1175 317–333. doi: 10.1029/JB086iB01p00317
- 1176 Wang, H., Yuan, L., Wang, L., Zhou, Z., & An, J. (2016). Very Low-Grade Meta-  
 1177 morphism of Clastic Rocks from the Meso-Neoproterozoic and the Paleozoic  
 1178 along the Profile Yueyang-Linxiang in Northeastern Hunan Province and Its  
 1179 Geological Implications. *Acta Geologica Sinica - English Edition*, 90(5), 1743–  
 1180 1753. doi: 10.1111/1755-6724.12813
- 1181 Wang, H., Zhou, Z., Wang, L., & Yuan, L. (2014). Anchimetamorphism and di-  
 1182 agenesis of the Meso-Neoproterozoic and the Lower Paleozoic along profile  
 1183 Yangjiaping in North Hunan Province, China. *Yanshi Xuebao/Acta Petrologica*  
 1184 *Sinica*, 30(10), 3013–3020.
- 1185 Wang, J., Li, X., Duan, T., Liu, D., Song, B., Li, Z., & Gao, Y. (2003). Zircon  
 1186 SHRIMP U-Pb dating for the Cangshuipu volcanic rocks and its implications  
 1187 for the lower boundary age of the Nanhua strata in South China. *Chinese*  
 1188 *Science Bulletin*, 48(16), 1663–1669. doi: 10.1360/03wd0168
- 1189 Wang, J., & Li, Z. X. (2003). History of neoproterozoic rift basins in South China:  
 1190 Implications for Rodinia break-up. *Precambrian Research*, 122(1-4), 141–158.  
 1191 doi: 10.1016/S0301-9268(02)00209-7
- 1192 Wang, J., Zhou, X., Deng, Q., Fu, X., Duan, T., & Guo, X. (2015). Sedimentary  
 1193 successions and the onset of the Neoproterozoic Jiangnan sub-basin in the  
 1194 Nanhua rift, South China. *International Journal of Earth Sciences*, 104(3),  
 1195 521–539. doi: 10.1007/s00531-014-1107-5
- 1196 Wang, W., Zhou, M. F., Zhao, J. H., Pandit, M. K., Zheng, J. P., & Liu, Z. R.  
 1197 (2016). Neoproterozoic active continental margin in the southeastern Yangtze  
 1198 Block of South China: Evidence from the ca. 830–810 Ma sedimentary strata.  
 1199 *Sedimentary Geology*, 342, 254–267. doi: 10.1016/j.sedgeo.2016.07.006
- 1200 Wang, Y., Fan, W., Zhao, G., Ji, S., & Peng, T. (2007). Zircon U-Pb geochronology  
 1201 of gneissic rocks in the Yunkai massif and its implications on the Caledonian  
 1202 event in the South China Block. *Gondwana Research*, 12(4), 404–416. doi:  
 1203 10.1016/j.gr.2006.10.003
- 1204 Watson, G. S., & Enkin, R. J. (1993). The fold test in paleomagnetism as a param-  
 1205 eter estimation problem. *Geophysical Research Letters*, 20(19), 2135–2137. doi:  
 1206 10.1029/93GL01901
- 1207 Widmann, P., Davies, J. H., & Schaltegger, U. (2019). Calibrating chemi-  
 1208 cal abrasion: Its effects on zircon crystal structure, chemical composition  
 1209 and U–Pb age. *Chemical Geology*, 511(February), 1–10. doi: 10.1016/  
 1210 j.chemgeo.2019.02.026
- 1211 Xian, H., Zhang, S., Li, H., Yang, T., & Wu, H. (2020). Geochronological and  
 1212 palaeomagnetic investigation of the Madiyi Formation, lower Banxi Group,  
 1213 South China: Implications for Rodinia reconstruction. *Precambrian Research*,  
 1214 336(July 2020), 105494. doi: 10.1016/j.precamres.2019.105494

- 1215 Xianqing, J., Yang, Z., Tong, Y., Wang, H., & Xu, Y. (2018). A SHRIMP U-Pb zir-  
 1216 con geochronology of a tuff bed from the bottom of Liantuo Formation in the  
 1217 Three Gorges area and its geological implications. *Journal of Jilin University*  
 1218 (*Earth Science Edition*), *48*(1), 165–180. doi: 10.13278/j.cnki.jjuese.20160232
- 1219 Xie, S.-k., Wang, Z.-j., Wang, J., & Zhuo, J.-w. (2012). LA-ICP-MS zircon U-Pb  
 1220 dating of the bentonites from the uppermost part of the Ordovician Wufeng  
 1221 Formation in the Haoping section, Taoyuan, Hunan. *Sedimentary and Tethyan*  
 1222 *Geology*, *4*, 597.
- 1223 Xu, Y. J., Cawood, P. A., & Du, Y. S. (2016). Intraplate orogenesis in response to  
 1224 Gondwana assembly: Kwangsi Orogeny, South China. *American Journal of*  
 1225 *Science*, *316*(4), 329–362. doi: 10.2475/04.2016.02
- 1226 Yan, D. P., Zhou, M. F., Song, H. L., Wang, X. W., & Malpas, J. (2003). Ori-  
 1227 gin and tectonic significance of a Mesozoic multi-layer over-thrust system  
 1228 within Yangtze Block (South China). *Tectonophysics*, *361*(3-4), 239–254. doi:  
 1229 10.1016/S0040-1951(02)00646-7
- 1230 Yang, J., Luo, P., Ling, Y., Yang, S., Bai, D., Wei, F., . . . Peng, N. (2021). Su-  
 1231 perimposed features and deformation mechanism of Early Mesozoic folds in  
 1232 the Sangzhi-Shimen area, northern Hunan. *Bulletin of Geological Science and*  
 1233 *Technology*, *40*(6), 43–54. doi: 10.19509/j.cnki.dzkq.2021.0605
- 1234 Yang, S. X., & Blum, N. (1999). A fossil hydrothermal system or a source-bed in the  
 1235 Madiyi Formation near the Xiangxi Au-Sb-W deposit, NW Hunan, PR China?  
 1236 *Chemical Geology*, *155*(1-2), 151–169. doi: 10.1016/S0009-2541(98)00146-6
- 1237 Yang, Z., Sun, Z., Yang, T., & Pei, J. (2004). A long connection (750–380 Ma) be-  
 1238 tween South China and Australia: Paleomagnetic constraints. *Earth and Plan-*  
 1239 *etary Science Letters*, *220*(3-4), 423–434. doi: 10.1016/S0012-821X(04)00053  
 1240 -6
- 1241 Yao, J., Cawood, P. A., Shu, L., & Zhao, G. (2019). Jiangnan Orogen, South China:  
 1242 A 970–820 Ma Rodinia margin accretionary belt. *Earth-Science Reviews*, *196*.  
 1243 doi: 10.1016/j.earscirev.2019.05.016
- 1244 Yin, C., Gao, L., Xing, Y., Wang, Z., & Tang, F. (2004). Advances in the study on  
 1245 the Nanhua System of the Neoproterozoic and its stratotype in South China  
 1246 (in Chinese with English abstract). In *Professional papers of stratigraphy and*  
 1247 *palaeontology* (pp. 1–10). Beijing: Geological Publishing House.
- 1248 Yin, C., Liu, D., Gao, L., Wang, Z., Xing, Y., Jian, P., & Shi, Y. (2003). Lower  
 1249 boundary age of the Nanhua System and the Gucheng glacial stage: Evidence  
 1250 from SHRIMP II dating. *Chinese Science Bulletin*, *48*(16), 1657–1662. doi:  
 1251 10.1360/03wd0112
- 1252 Zhang, H. (1998). Preliminary Proterozoic apparent polar wander paths for the  
 1253 South China Block and their tectonic implications. *Canadian Journal of Earth*  
 1254 *Sciences*, *35*(3), 302–320. doi: 10.1139/e97-117
- 1255 Zhang, Q. R., & Piper, J. D. (1997). Palaeomagnetic study of Neoproterozoic glacial  
 1256 rocks of the Yangzi Block: Palaeolatitude and configuration of South China in  
 1257 the late Proterozoic Supercontinent. *Precambrian Research*, *85*(3-4), 173–199.
- 1258 Zhang, S., Chang, L., Zhao, H., Ding, J., Xian, H., Li, H., . . . Yang, T. (2021). The  
 1259 Precambrian drift history and paleogeography of the Chinese cratons. In *An-*  
 1260 *cient supercontinents and the paleogeography of earth* (pp. 333–376). Elsevier.  
 1261 doi: 10.1016/B978-0-12-818533-9.00005-9
- 1262 Zhang, S., Jiang, G. Q., Dong, J., Han, Y. G., & Wu, H. C. (2008). New SHRIMP  
 1263 U-Pb age from the Wuqiangxi Formation of Banxi Group: Implications for rift-  
 1264 ing and stratigraphic erosion associated with the early Cryogenian (Sturtian)  
 1265 glaciation in South China. *Science in China, Series D: Earth Sciences*, *51*(11),  
 1266 1537–1544. doi: 10.1007/s11430-008-0119-z
- 1267 Zhang, S., Li, H., Jiang, G., Evans, D. A., Dong, J., Wu, H., . . . Xiao, Q. (2015).  
 1268 New paleomagnetic results from the Ediacaran Doushantuo Formation in  
 1269 South China and their paleogeographic implications. *Precambrian Research*,

- 1270 259, 130–142. doi: 10.1016/j.precamres.2014.09.018
- 1271 Zhang, S., Li, H., Zhang, X., Wu, H., Yang, T., Liu, Y., & Cao, Q. (2012). New  
1272 Ordovician paleomagnetic results from South China Block and their paleogeo-  
1273 graphic implications. *The 34th IGC abstract*.
- 1274 Zhang, X., Wang, Y., & Chen, X. (2000). Diagenesis and Porosity of the Cambrian-  
1275 Ordovician Carbonate Shoal Facies at Yangjiaping, Shimen, Hunan. *Acta Ge-  
1276 ologica Sinica - English Edition*, 74(1), 29–45. doi: 10.1111/j.1755-6724.2000  
1277 .tb00429.x
- 1278 Zhang, Y., Wang, Y., Zhang, Y., & Zhang, A. (2015). Neoproterozoic assembly of  
1279 the Yangtze and Cathaysia blocks: Evidence from the Cangshuipu Group and  
1280 associated rocks along the Central Jiangnan Orogen, South China. *Precam-  
1281 brian Research*, 269, 18–30. doi: 10.1016/j.precamres.2015.08.003
- 1282 Zhao, G., Wang, Y., Huang, B., Dong, Y., Li, S., Zhang, G., & Yu, S. (2018). Geo-  
1283 logical reconstructions of the East Asian blocks: From the breakup of Rodinia  
1284 to the assembly of Pangea. *Earth-Science Reviews*, 186(October), 262–286.  
1285 doi: 10.1016/j.earscirev.2018.10.003
- 1286 Zheng, B., Zhou, R., Mou, C., Wang, X., Xiao, Z., & Chen, Y. (2020). Nature of  
1287 the Late Ordovician-Early Silurian Xiaohe section, Hunan-Hubei area, South  
1288 China: implications for the Kwangsi Orogeny. *International Geology Review*,  
1289 62(10), 1262–1272. doi: 10.1080/00206814.2019.1644541
- 1290 Zijderveld, J. (1967). A.C. demagnetization of rocks: Analysis of results. In S. Run-  
1291 corn, K. Creer, & D. Collinson (Eds.), *Methods in palaeomagnetism* (pp. 254–  
1292 286). Amsterdam: Elsevier.

## Appendix A Supplementary figures and tables

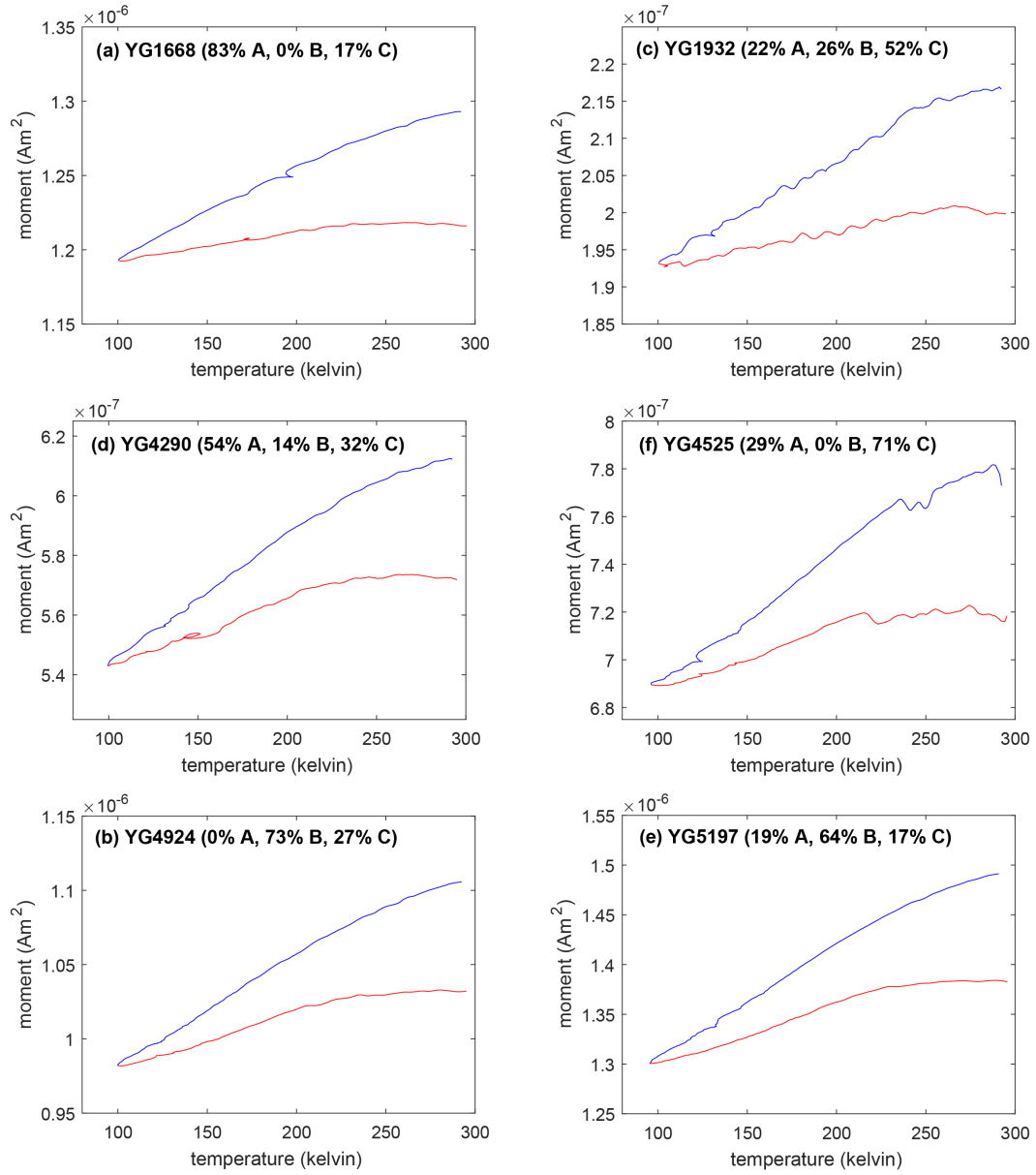


**Figure A1.** Examples of low temperature remanence curves for component groups A, (a) and (d), B (b) and (e), and C, (c) and (f). Experiments were performed on crushed specimens in air between room temperature (293 K) and  $-273^\circ\text{C}$  (100 K). Blue lines are cooling curves and red lines are warming curves. All measured specimens show neither a Morin nor a Verwey transition.

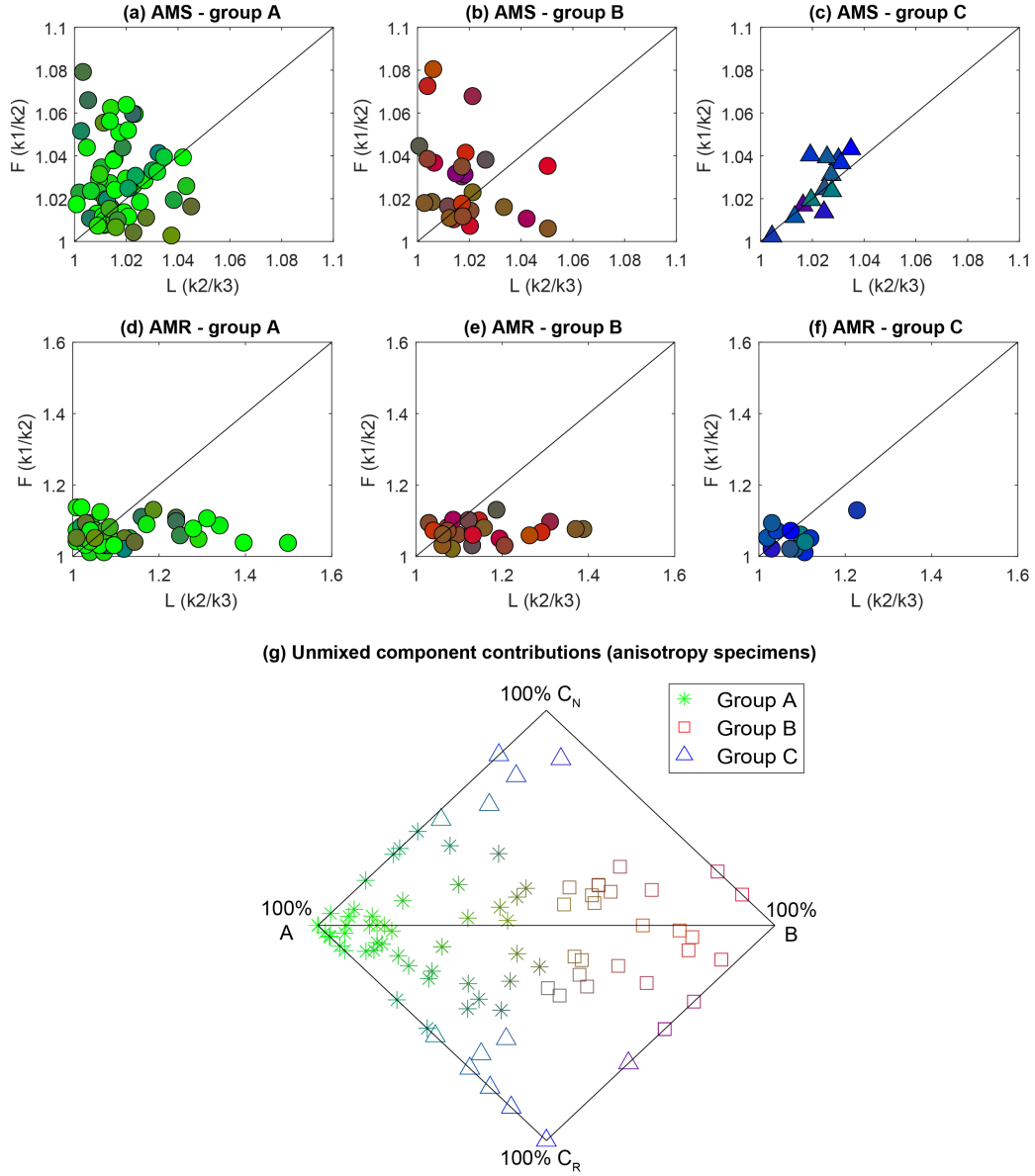


**Figure A2.** Flinn (1962) diagrams by component group for AMS (a-c) and AMR (d-f), with points shaded by component contributions estimated from vector unmixing analyses (g). Note the significant difference in axes on Flinn diagrams between AMS and AMR.

**Table A1.** Tonian poles for the SCB (820–720 Ma). ID' = pole derived with shallowing correction. ID\* = recalculated pole excluding rotated sites (see text).  $A_{95}$  = radius of 95% confidence circle for mean pole. dp and dm = semi-axes of the 95% confidence ellipse. f = flattening factor for shallowing correction. R following Meert et al. (2020).

Formation	ID	age (Ma)	site lat.	site lon.	pole lat.	pole lon.	$A_{95}$ (dp/dm)	f	criteria	R	†age ref./ <sup>+</sup> pole ref.
Xiaofeng dykes	XF	821 ± 0.2	31.0	111.2	13.5	91.0	10.5/11.3	-	1100100	3	†W. Wang et al. (2016)/ <sup>+</sup> Z. X. Li et al. (2004)
	XF*	802 ± 10			26.1	82.1	14.0/15.2	-			†Z. X. Li et al. (2004)/ <sup>+</sup> Jing et al. (2020)
Yanbian dykes	YB1	824 ± 6	26.9	101.5	45.1	130.4	19.0	-	1110001	4	†+Niu et al. (2016)
	YB2	806 ± 8	26.9	101.5	14.1	32.5	20.4	-	1011000	3	†+Niu et al. (2016)
Madiyi Fm.	MD	805 ± 1	27.5	109.6	35.3	67.9	4.7/5.5	1	1010110	4	†Park et al. (2021)/ <sup>+</sup> Xian et al. (2020)
	MD'				34.3	82.4	3.7/3.9	0.6			+Park et al. (2021)
Chengjiang Fm.	CJ1	800 ± 8.4	25.2	102.4	32.8	56.3	8.1/8.6	1	1011010	4	†+Jing et al. (2020)
	CJ1'				29.7	75.3	7.9	0.6			+Park et al. (2021)
Liantuo Fm.	CJ3	785 ± 12	25.2	102.4	22.6	33.2	9.5/14.8	1	1010000	2	†+Jing et al. (2020)
	LT1	780 ± 0.9	30.8	110.9	20.0	148.7	8.7/10.0	1	1011011	5	†Park et al. (2021)/ <sup>+</sup> Jing et al. (2021)
	LT1'				24.9	136.4	6.6	0.6			+Park et al. (2021)
	LT2	ca. 720	30.8	111.1	12.2	155.2	5.3/5.2	1	0010011	3	†Park et al. (2021)/ <sup>+</sup> Jing et al. (2015)
Xiajiang Gp.	LT2'				19.6	144.4	4.2	0.6			+Park et al. (2021)
	XJ	816–810	27.9	108.8	50.7	100.0	12.3	1	1011011	5	+Park et al. (2021)/(recalculated)
Guzhang/Anjiang Laoshanya Fm.	XJ'				42.7	104.0	8.1	0.6			†+Park et al. (2021)
	GA	ca. 770	28.5	109.8	25.6	116.8	9.9	-	0111111	6	†+Chang et al. (2022)
	LS-C	807.5 ± 0.2	30.0	110.7	53.9	136.2	4.5/5.0	1	1110111	6	This study (tilt-corrected)

**Table A2.** Cambrian to Silurian (635 – 420 Ma) study poles for the SCB used in this study.

Formation (locality)	ID	age	site		site		pole lat.	pole lon.	$A_{95}$ (dp/dm)	references
			lat.	lon.	lat.	lon.				
(Shiqian, Guizhou)	SQ	S	27.5	108.0	14.9	196.1	5.1	K. Huang et al. (2000); B. Huang et al. (2018)		
(Xiushan, Sichuan)	XS	S	28.5	109.0	6.8	195.7	5.4	Opdyke et al. (1987); B. Huang et al. (2018)		
Pagoda (Wangcang)	PG	O	32.4	106.3	-45.8	191.3	2.4/4.2	Han et al. (2015); S. Zhang et al. (2015)		
Baota (Shanxi)	BS	O	-	-	-29.5	227.0	6.3	S. Zhang et al. (2012, 2015)		
Hongshiya (Yunnan)	HF	O	25.6	102.6	-38.9	235.7	16.9	Fang et al. (1990); B. Huang et al. (2018)		
Hongshiya (Yunnan)	HG	O	25.6	102.5	-48.1	229.4	4.4	Gao et al. (2018)		
Duoposi (Wangcang)	DW	C	32.1	106.2	-39.5	185.1	4.4/8.3	Bai et al. (1998); B. Huang et al. (2018)		
Duoposi (Guangyuan)	DG	C	32.4	106.3	-51.3	166.0	4.4/8.6	Z. Yang et al. (2004); B. Huang et al. (2018)		
Doushantuo (Jiulongwan)	DJ	Ed	30.8	111.1	23.9	187.0	1.8/3.0	S. Zhang et al. (2015)		
Doushantuo (Yangjiaping)	DY	Ed	30.0	110.7	0.6	196.9	4.5/9.0	Macouin et al. (2004)		
Laoshanya (Yangjiaping)	LS-B	O?	30.0	110.7	-49.8	209.9	3.1/4.8	This study (tilt-corrected)		

S = Silurian, O = Ordovician, C = Cambrian, Ed = Ediacaran

**Table A3.** Site directions for component C from the Laoshanya Formation. Specimens were grouped into stratigraphic units of  $n = 8-12$  for comparison with other studies.  $n/N =$  number of specimens/sites.  $D_g/I_g$  and  $D_s/I_s =$  geographic (in situ) and stratigraphic (tilt-corrected) declination/inclination.  $\kappa$  and  $\alpha_{95}$  are the precision parameter and 95% confidence circle (Fisher, 1953).

site	height (m)	n	$D_g$	$I_g$	$D_s$	$I_s$	$\kappa$	$\alpha_{95}$
C1	02.2 - 25.8	12	337.2	-46.6	185.2	-74.3	62.6	5.5
C2	29.1 - 32.8	8	146.3	39.4	43.8	73.1	45.6	8.3
C3	36.4 - 38.8	8	154.2	31.3	76.4	80.8	25.8	11.1
C4	44.9 - 46.6	11	146.6	45.5	26.3	70.4	71.8	5.4
C5	46.6 - 47.8	11	146.1	49.9	17.8	67.3	54.9	6.2
C6	47.8 - 48.9	11	144.6	47.8	23.5	67.9	92.5	4.8
C7	49.4 - 52.1	10	152.3	39.4	35.7	77.3	51.8	6.8
C8	52.1 - 84.1	10	327.2	-33.5	244.7	-75.0	15.4	12.7
mean		(N=8)	149.4	41.7	32.5	74.2	112.6	5.2

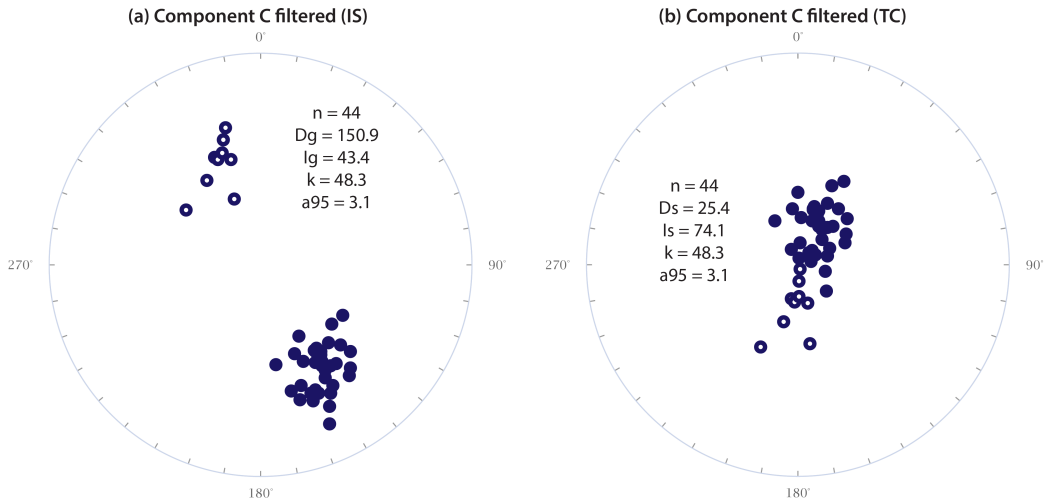


**Figure A3.** Component C specimen directions after filtering for results which decay to the origin on a Zijderveld plot and have  $MAD < 10^\circ$ , presented in (a) geographic (IS) and (b) stratigraphic (TC) coordinates. The directions pass a reversal test with a 'B' classification (McFadden & McElhinny, 1990).

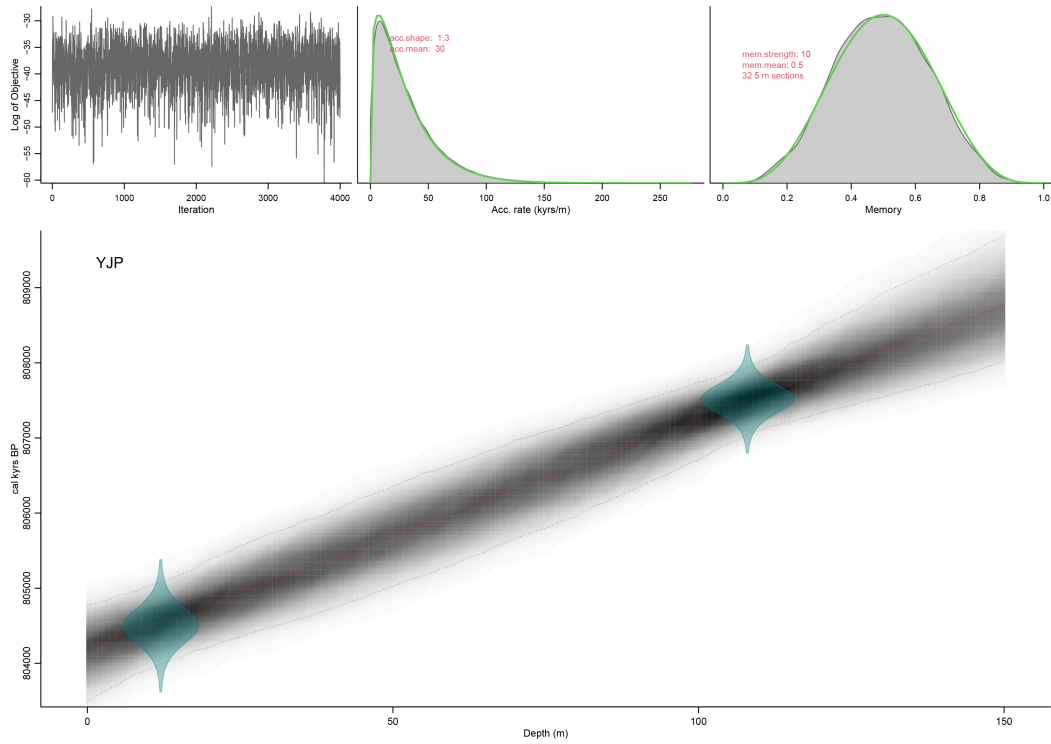


**Figure A4.** Age-depth model for the Laoshanya Formation in Yangjiaping, based on CA-ID-TIMS dating of two intercalated tuff beds, calculated using the approach of Blaauw and Christeny (2011). With linear extrapolation, assuming a constant accumulation rate, the results suggest that the formation was deposited between 808.7 [median, 95% range = 809.6 – 808.0] and 804.2 [median, 95% range = 804.7 – 803.5] Ma.

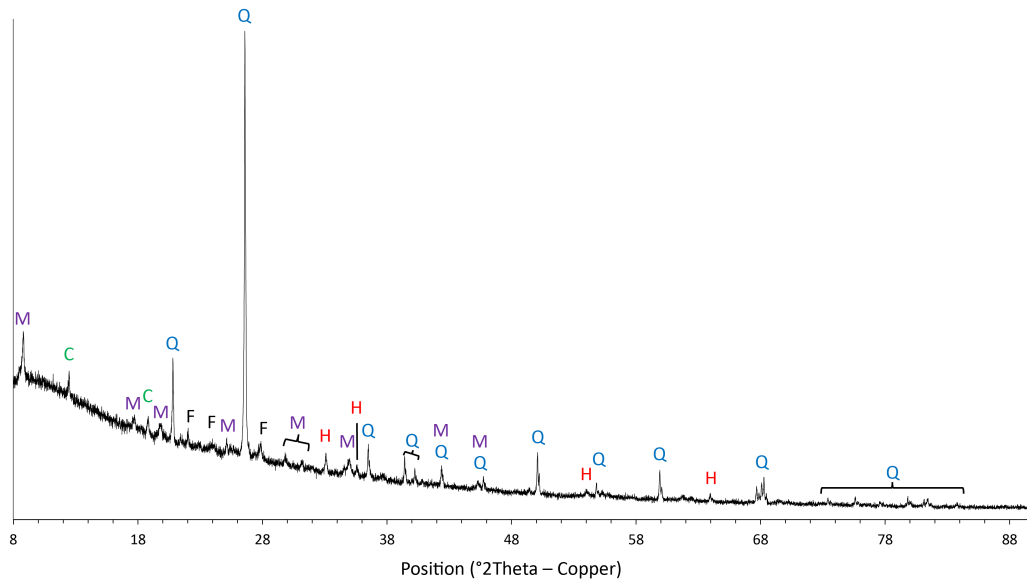


**Figure A5.** Typical diffractogram of Laoshanya rock powder (sample YG1120) highlighting the location of diffraction peaks from the different minerals. Abbreviations for the phases are: Q: quartz; M: muscovite; F: feldspar; C: chlorite; H: hematite.

## 1294 **Appendix B Review of Tonian poles for the SCB (820–720 Ma)**

1295 Here we present a review of all known 820 – 720 Ma paleopoles for South China.  
 1296 Each pole is assessed using the updated ‘R’ quality criteria of Meert et al. (2020). A sum-  
 1297 mary of the assessment is given in Table A1.

### 1298 ***B01 Xiaofeng dykes (XF)***

1299 Z. X. Li et al. (2004) reported a pole from the Xiaofeng dykes (XF), which were  
 1300 SHRIMP dated at  $802 \pm 10$  Ma. W. Wang et al. (2016) redated the dykes to  $821.6 \pm$   
 1301  $0.2$  Ma with laser ablation (LA-) MC-ICP-MS. However, Jing et al. (2020) noted that  
 1302 W. Wang et al. (2016) dated material from felsic dykes which were cut by younger mafic  
 1303 dykes, while the paleomagnetic data were obtained mainly from mafic dykes, so the older  
 1304 age of W. Wang et al. (2016) may not relate to the same rocks used for paleomagnetism.  
 1305 Jing et al. (2020) observed two groups of directions within the dykes, coming from op-  
 1306 posite sides of a fault. They recalculated a pole after excluding one subgroup deemed  
 1307 to be locally rotated. Therefore, we prefer the younger age of  $802 \pm 10$  Ma (Z. X. Li et  
 1308 al., 2004) and the recalculated (XF\*) pole of Jing et al. (2020). The pole, when reversed,  
 1309 lies close to Early Paleozoic poles (Fig. 14).

### 1310 ***B02 Yanbian dykes (YB)***

1311 Niu et al. (2016) presented poles from two groups of the mafic Yanbian dykes, dated  
 1312 at  $824 \pm 6$  Ma (YB1) and  $806 \pm 8$  Ma (YB2) via secondary ion mass spectrometry (SIMS).  
 1313 A vertical axis rotation of  $5^\circ$  was subtracted, based on paleomagnetic data from nearby  
 1314 Pliocene rocks. Park et al. (2021) excluded both poles from their compilation, observ-  
 1315 ing that no tilt correction was applied to most of the dykes (despite that several dip up  
 1316 to  $43^\circ$  from vertical) and that the dykes may have experienced vertical axis rotation prior  
 1317 to the Pliocene.

### 1318 ***B03 Madiyi Formation (MD)***

1319 Xian et al. (2020) reported a pole from Madiyi silty mudstones, initially dated with  
 1320 SIMS at  $802 \pm 6$  Ma, but redated to  $805 \pm 1$  Ma by CA-ID-TIMS (Park et al., 2021).  
 1321 The data in Xian et al. (2020) had no independent field tests to constrain the relative  
 1322 age of magnetization. A flattening factor of 0.6 was applied to correct for inclination shal-  
 1323 lowing, with no justification (E/I or anisotropy not measured/calculated). The original  
 1324 pole (uncorrected for inclination shallowing) lies close to Early Paleozoic poles when plot-  
 1325 ted in the southern hemisphere (Fig. 14). We note that the antipodal directions passed  
 1326 a reversal test, but only when applied on a subset of directions.

### 1327 ***B04 Chengjiang Formation (CJ)***

1328 Jing et al. (2020) reported two poles (CJ1 and CJ3) from Chengjiang Formation  
 1329 red sandstones, dated by SHRIMP at  $800 \pm 8$  Ma (CJ1) and  $785 \pm 12$  Ma (CJ3). The  
 1330 Chengjiang Formation was correlated with the Wuqiangxi Formation, which overlies the  
 1331 Madiyi Formation (Jiang et al., 2012). Thermal demagnetization data passed a fold test  
 1332 at 99% confidence limits (Jing et al., 2020). Park et al. (2021) recalculated an inclina-  
 1333 tion corrected pole by applying a flattening factor of 0.6 with no justification. The CJ1  
 1334 pole of Jing et al. (2020) overlaps with younger Ordovician poles (Fig. 14).

### 1335 ***B05 Liantuo Formation (LT)***

1336 Jing et al. (2021) reported the most recent pole (LT1) from sandstones of the lower  
 1337 Liantuo Formation, although there have been several other studies (Q. R. Zhang & Piper,  
 1338 1997; Evans et al., 2000; Jing et al., 2015). The LT1 pole was assigned an age of  $760 \pm$

1339 10 Ma by (Jing et al., 2021), based a range of dates obtained by the SIMS and SHRIMP  
 1340 methods (Lan et al., 2015; Xianqing et al., 2018), subsequently revised to  $779.5 \pm 0.9$   
 1341 Ma by Park et al. (2021) using ID-TIMS.

1342 Previously, Jing et al. (2015) reported a pole from sandstones in the upper Liantuo  
 1343 Formation (LT2), combined with the earlier pole of Evans et al. (2000). The age of the  
 1344 LT2 pole was revised to  $720 \pm 15$  Ma by Lan et al. (2015) using SIMS, although this age  
 1345 is contentious; Evans et al. (2000) originally assigned a SHRIMP age of  $748 \pm 12$  Ma (Ma  
 1346 et al., 1984).

#### 1347 ***B06 Xiajiang Group (XJ)***

1348 Park et al. (2021) reported several poles from fine-grained siliclastic sediments of  
 1349 the Xiajiang Group as well as high-precision U-Pb CA-ID-TIMS ages from interbedded  
 1350 tuffs. However, there was limited assessment of remanence carriers and no assessment  
 1351 of inclination shallowing. The pole reported by Park et al. (2021) is a study mean which  
 1352 averages data across several sites, with ages spanning more than 11 Myr ( $815.7 - 804.6$   
 1353 Ma), and there are significant directional differences between sites.

#### 1354 ***B07 Guzhang and Anjiang sills (GA)***

1355 Chang et al. (2022) reported a pole from mafic sills intruding the Banxi Group with  
 1356 loose age constraints ca. 770 Ma. One of the Guzhang dolerite dykes was dated at  $768$   
 1357  $\pm 28$  Ma using the SHRIMP method, while ages for the Anjiang dykes range from 775  
 1358 to 791 Ma. The pole is statistically robust and passes field and reversal tests, but has a  
 1359 large age uncertainty ( $> 15$  Myr).

#### 1360 ***B08 Laoshanya Formation (LS)***

1361 We define a new Tonian pole (LS-C) based on the tilt-corrected mean direction of  
 1362 group C specimens of the Laoshanya Formation ( $n = 81$ ). The pole is statistically ro-  
 1363 bust and passes a reversal test when filtered for the highest quality directions (linear de-  
 1364 cay to origin,  $MAD < 10^\circ$ ,  $n = 44$ ). The pole is unique from any younger poles (Fig.  
 1365 12). We were unable to obtain independent field (fold, contact or conglomerate) tests,  
 1366 but our observations in Section 4 suggest that the paleomagnetic signal is primary. There-  
 1367 fore, we assign the pole an age of  $807.5 \pm 0.2$  Ma (Section 4.1).

#### 1368 ***B09 Cambrian to Paleozoic poles***

1369 In Table A2, we list Cambrian to Paleozoic poles for the SCB (B. Huang et al., 2018),  
 1370 as well as Ediacaran poles of Macouin et al. (2004) and S. Zhang et al. (2015), and Or-  
 1371 dovician poles from the Baota (S. Zhang et al., 2012) and Hongshiya (Gao et al., 2018)  
 1372 Formations. All poles are derived in tilt-corrected coordinates.